Most root-derived carbon inputs do not contribute to the global bulk soil carbon pool

Authors: Guocheng Wang[1,2]†, Liujun Xiao[2]†, Xiali Mao[2], Xiaowei Guo[2], Annette Cowie[3], Shuai Zhang[2], Mingming Wang[2], Songchao Chen[4], Ganlin Zhang[5], Zhou Shi[2], Zhongkui Luo[2]*

Affiliations: [1]State Key Laboratory of Atmospheric Boundary Layer Physics and Atmospheric Chemistry, Institute of Atmospheric Physics, Chinese Academy of Sciences, Beijing 100029, China; [2]College of environmental and resource sciences, Zhejiang University, Hangzhou, Zhejiang 310058, China; [3]New South Wales Department of Primary Industries/University of New England, Armidale, NSW 2351, Australia; [4]INRAE Unité InfoSol, Orléans 45075, France; [5]State Key Laboratory of Soil and Sustainable Agriculture, Institute of Soil Science, Chinese Academy of Sciences, Nanjing, Jiangsu 210008, China; †These authors contributed equally; *email: luozk@zju.edu.cn

Plant root-derived carbon (C) inputs (I_{root}) are the primary source of C in mineral bulk soil. However, a fraction of I_{root} may lose directly (I_{loss}, e.g., via rhizosphere microbial respiration, leaching and fauna feeding) without contributing to bulk soil C pool. This loss has never been quantified, particularly at global scale, inhibiting reliable estimation of soil C dynamics. Here we integrate three observational global datasets including radiocarbon content, allocation of photosynthetically assimilated C, and root biomass distribution in 2,034 soil profiles to quantify I_{root} and its contribution to the bulk soil C pool. We show that global average I_{root} in the 0-200 cm soil profile is 3.5 Mg ha^{-1} yr^{-1}, ~80% of which (i.e., I_{loss}) is lost rather than entering bulk soil. If ignoring I_{loss}, bulk soil C turnover will be incorrectly estimated to be four times faster. This can explain why Earth system models (in which all I_{root} enters bulk soil C pools) predict much faster soil C turnover than radiocarbon-constrained estimates. I_{root} decreases exponentially with soil

depth, and the top 20 cm soil contains >60% of total I_{root}. Actual C input to bulk soil (i.e., $I_{root} - I_{loss}$) shows a similar depth distribution to I_{root}. We also map I_{loss} and its depth distribution across the globe. Our results demonstrate the global significance of direct C losses which limit the contribution of I_{root} to bulk soil C storage; and provide spatially explicit data to facilitate reliable soil C predictions via separating direct C losses from total root-derived C inputs.

Globally, mineral soil is the largest terrestrial carbon (C) reservoir, mediating C exchanges among other C reservoirs particularly the atmosphere and water bodies (e.g., rivers, lakes, groundwater and oceans)[1,2]. Soil receives photosynthetically assimilated C (i.e., organic carbon inputs) and releases C mainly via microbial decomposition (i.e., heterotrophic respiration outputs). Both C inputs and outputs to the soil system, the balance of which determines soil C stocks, are influenced by various environmental factors[1,3,4], resulting in great spatial and temporal variability of soil C stocks down the soil profile as well as across the globe[5,6]. While bulk soil C stock is relatively easy to measure via sampling soil cores, the determination of C inputs and outputs is not that straightforward. Indeed, *in situ* quantification of C outputs in the form of CO_2 from the bulk soil is a grand challenge because CO_2 emissions from the soil are comprised of heterotrophic respiration by decomposers and root autotrophic respiration, which are difficult, if not impossible, to separate[7]. An even harder question is how to partition CO_2 emissions to different soil depths where CO_2 is produced. Our poor knowledge of C inputs to and outputs from different soil depths inhibits understanding of whole-soil profile C dynamics in response to environmental change factors[8,9] and management[10,11].

Compared to challenges of quantifying C outputs and their depth-origin, C inputs to the soil can be represented by root-derived C and reasonably estimated using state-of-the-art tracer (e.g., C isotopes) techniques[8] or by root growth measurements[12-14]. Numerous relevant data

have been collected in the last decades[15], and used to estimate soil C turnover based on the ratio of soil C stocks to C inputs under the assumption of steady state[15,16]. Alternatively, radiocarbon-inferred C age can be used to estimate soil C turnover time[8,10,17], which is equivalent to C age[18]. In theory, soil C turnover times estimated by the two approaches should be the same or similar at least, but, surprisingly, have nearly an order of magnitude difference[8,10,15,17,19,20]. For example, the average turnover time of soil C in the 30-100 cm soil layer across the globe is estimated to be ~1,000 years based on belowground C allocation[15], and >8,000 years through radiocarbon[17]. An immediate question is: why? A possible explanation for this contrast is the steady state assumption adopted by both approaches, because real systems are transient, particularly in this anthropogenic era with significant perturbations. However, both empirical and modelling studies have demonstrated that the consequences of the steady state assumption on the millennial C turnover are minimum[8,21]. Another possibility is that plant-derived C inputs only participate in the cycling of a small fraction of total soil C pool[10,17]. This explanation is mechanistically possible but has not been tested at global scale, and conflicts with the common assumption that both methods estimate the average turnover time of soil C pool.

Here we propose that the apparent root-derived C inputs (I_{root}) does not equal actual C inputs to bulk soil (I_{bulk}) because there is a "leaky bridge" connecting I_{root} and I_{bulk}. This "bridge" may be the rhizosphere or other direct C loss pathways, where direct C efflux (e.g., volatile root exudates[22]) and/or transformation (e.g., microbial decomposition and root herbivore consumption[23]) processes are active, reducing the transfer of I_{root} to bulk soil[24]. The importance of direct C loss pathways such as rhizosphere processes in controlling soil C dynamics has been acknowledged[24-27]. However, in practice the extent to which the pathways modulate C inputs to bulk soil is rarely considered, mainly due to the difficulty of *in situ* measurement. Earth system models, the common tool for soil C projections at global scale, simply partition I_{root} into

one or several conceptual C pools in bulk soil[10,11], which may underestimate immediate turnover rates of I_{root} before entering the bulk soil[28] thereby overestimating the contribution of I_{root} to the bulk soil C pool. In this study, we first quantify the global pattern of I_{root} and I_{bulk} and their drivers, and then estimate the "leaked" amount of I_{root} [i.e., the direct C loss via various pathways (I_{loss})] as: $I_{root} - I_{bulk}$. At last, taking advantage of the data sources, we map I_{loss} across global terrestrial soils at the resolution of 1 km.

Root-derived C inputs (I_{root})

The input of root-derived C to soil (I_{root}) can be estimated by combining plant net primary productivity (NPP, i.e., the difference between photosynthesized and respired C) and its belowground allocation (f_{BNPP}): $I_{root} = NPP \times f_{BNPP}$. We compiled a comprehensive dataset of NPP enabling the calculation of f_{BNPP} from field measurements at 725 sites across the globe (i.e., NPP_{data} hereafter; Methods, Extended Data Fig. 1) to assess the global pattern and underlying drivers of I_{root}. Averaged across 725 sites in the 0-200 cm soil profile, I_{root} is 3.50 Mg ha^{-1} yr^{-1} ranging from 0.09 [2.5% confidence intervals (CI)] to 13.38 Mg ha^{-1} yr^{-1} (97.5% CI, Fig. 1a). The proportional belowground allocation of total NPP (i.e., f_{BNPP}) averages 37.7%, ranging from 7.6% to 82.7% (Fig. 1c). Among biomes, I_{root} is significantly different ($P < 0.05$, Fig. 1a). Mediterranean/montane shrublands have the highest I_{root} (5.42 Mg ha^{-1} yr^{-1}), followed by cropland (4.42 Mg ha^{-1} yr^{-1}); tundra has the lowest (0.90 Mg ha^{-1} yr^{-1}), followed by boreal forests (2.36 Mg ha^{-1} yr^{-1}, Fig. 1a). f_{BNPP} is >50% in temperate grasslands, deserts and Mediterranean/montane shrublands, but only ~30% in tropical/subtropical forests, temperate forests and boreal forests (Fig. 1c and Supplementary Fig. 1).

With respect to depth distribution of I_{root}, the allocation to the 0-20 cm soil layer is 2.43 Mg ha^{-1} yr^{-1} on average across all sites (Fig. 1b), accounting for 60% of total I_{root} (Fig. 1d), and >80% I_{root} is allocated to the top 60 cm soil layer (Fig. 1d). Among biomes, depth

distribution of I_{root} differs significantly ($P < 0.05$, Supplementary Fig. 2). For example, boreal forests and tundra have much higher allocation to top layers (e.g., 0-20 cm) than deserts and temperate forests. The different depth distribution of I_{root} reflects the general soil moisture pattern among biomes. That is, roots go to deeper to find moisture in drier environments[29]. In tundra, permafrost inhibits root growth into the subsoil[30], resulting in large fraction of I_{root} allocated to surface layers.

Focusing on the variability of total I_{root} across the 725 sites, we assess the underlying environmental drivers including climatic, edaphic and topographic variables, and biome type (Supplementary Table 1), using a multivariate linear mixed regression treating biome type as a random effect (Methods). The regression explains 50% of the variance of global I_{root} (Fig. 2). Soil and climate show similar overall importance, but are more important than topography. The regression coefficients indicate that the drivers differ within each biome (Fig. 2), reflecting the strong dependence of environmental controls on biome type. These results demonstrate that I_{root} is driven by complex interplay among edaphic, climatic and topographic variables, which is further modulated by biome type as different biomes may adopt distinct NPP allocation strategies[31-33].

Carbon inputs to bulk soil (I_{bulk})

Radiocarbon ($\Delta^{14}C$) measurements in bulk soil provide the opportunity to inversely estimate actual C inputs to bulk soil (I_{bulk}, Methods). We first used the ISRaD[34] radiocarbon dataset ($\Delta^{14}C_{data}$) to calculate soil C ages[35-37] (C_{age}) in 750 soil profiles across the globe (Extended Data Fig. 1) using a radiocarbon model (Methods) together with historical atmospheric radiocarbon concentration since 1950 (Supplementary Fig. 5a). The results indicate that the average C_{age} in the 0-200 cm soil profile across the 750 soil profiles is 3,862 years (Supplementary Fig. 5b). Using a similar dataset, Shi et al[17] estimated a global average C_{age} of 1,390 years in the 0-30

cm soil layer, which is generally in line with our estimation of 982 years for that soil depth. In the 30-100 cm soil layer, however, their estimation is 8,280 years, while ours is much younger at an average of 3,869 years. This discrepancy could be due to the estimation by Shi et al[17] being the global average based on global mapping product of $\Delta^{14}C$, while our results are based on original $\Delta^{14}C$ observations in the 750 soil profiles which include few samples in tundra and permafrost regions (Extended Fig. 1) where soil C usually has much longer turnover times than other regions[17].

Based on the $\Delta^{14}C$-dervied C_{age} and soil C stock (C_{stock}) measured with $\Delta^{14}C$ (Methods), we can estimate C inputs to bulk soil (I_{bulk}) in each soil layer for $\Delta^{14}C_{data}$ profiles as C_{stock}/C_{age} under the steady state assumption (Methods). Averaging across the 750 soil profiles in the 0-200 cm soil profile, I_{bulk} is 0.60 Mg ha^{-1} yr^{-1} ranging from 0.06 (2.5% CI) to 3.59 Mg ha^{-1} yr^{-1} (97.5% CI, Fig. 1a); and is significantly different among global biomes (Fig. 1a). Temperate forests have the highest I_{bulk} (1.20 Mg ha^{-1} yr^{-1}), followed by boreal forests (0.77 Mg ha^{-1} yr^{-1}); and deserts have the lowest I_{bulk} (0.16 Mg ha^{-1} yr^{-1}), followed by tundra (0.26 Mg ha^{-1} yr^{-1}, Fig. 1a). The depth distribution of I_{bulk} is generally consistent with that of I_{root} (Fig. 1b and d). On average, the results indicate 0.26, 0.06 and 0.03 Mg ha^{-1} yr^{-1} of I_{bulk} in the 0-20 cm, 20-40 cm and 40-60 cm soil layers, respectively (Fig. 1b), accounting for 68.9%, 14.1%, and 5.2% of total I_{bulk}, respectively (Fig. 1d). Across all biomes, I_{bulk} is significantly lower than I_{root} (Fig. 1a). As expected, depth is the dominant control on I_{bulk} in different soil layers (Fig. 2). The multivariate linear mixed regression considering soil depth, edaphic, climatic and topographic variables, and biome type (Methods) explains 74% of the variance of I_{bulk} (Fig. 2). Compared to the effects of environmental factors on I_{root}, their effects on I_{bulk} are more consistent among biome types. In addition, the three groups of environmental factors (i.e., edaphic, climatic and topographic) show similar overall importance for controlling I_{bulk} (Fig. 2).

Loss of root-derived C inputs (I_{loss})

Using the estimates of I_{root} and I_{bulk}, we can calculate the difference between I_{root} and I_{bulk} (i.e., $I_{root} - I_{bulk}$), which represents the loss of root-derived C inputs (I_{loss}) that leaves the soil via any direct loss pathways without entering the bulk soil and participating in the C cycle there. Considering potential uncertainties in NPP thus I_{root} and its allocation to soil depths, we conducted six independent estimates of I_{loss} based on four independent datasets (Methods, Extended Data Table 1) to provide confidence in the estimate of I_{loss} (Fig. 3, Supplementary Table 2 and Table 3).

Across the globe, the six independent estimates of I_{loss} are generally comparable, with an average of 2.31 Mg ha^{-1} yr^{-1} in the 0-200 cm soil profile (Fig. 3a), ranging from 1.80 to 3.36 Mg ha^{-1} yr^{-1} across different estimates (Supplementary Table 2). This average I_{loss} accounts for 77.9% of I_{root} ranging from 65.3% to 90.9% among the six estimates (Fig. 3c and Supplementary Table 2), demonstrating that most I_{root} does not enter bulk soil. Among biome types, I_{loss} is significantly different ($P < 0.05$, Fig. 3a and Supplementary Table 2). On average, tropical/subtropical forests have the largest I_{loss} of 3.30 Mg ha^{-1} yr^{-1}, followed by crops (2.74 Mg ha^{-1} yr^{-1}); and tundra has the smallest I_{loss} (0.66 Mg ha^{-1} yr^{-1}), followed by boreal forests (1.35 Mg ha^{-1} yr^{-1}, Fig. 3a). With respect to depth distribution, the average I_{loss} is 1.45, 0.44 and 0.16 Mg ha^{-1} yr^{-1} in the 0-20 cm, 20-40 cm and 40-60 cm soil layer respectively (Fig. 3b), accounting for 61.8%, 19.1% and 7.2% of total I_{loss} in the 0-200 cm soil profile, respectively (Fig. 3d). Depth distributions of I_{loss} quantified by the six independent estimates are also generally comparable (Figs. 3b and d), verifying the robustness of the estimation of I_{loss}. We note that I_{loss} is negative in some situations (Figs. 3a and b), which is possible if there is significant downward movement of C in the soil profile[38]. For example, the top mineral soil layer would receive C from organic matter on soil surface due to downward movement of

dissolved and particulate C, or soil mixing through bioturbation. For this reason, I_{bulk} in that layer may include illuvial C or other non-root-derived C.

We developed ensemble models based on five machine learning algorithms to predict I_{root}, I_{bulk} and their depth distributions (Methods). Independent validation of the derived machine learning models indicates that the I_{root} and I_{bulk} models are accurate (Extended Data Figs. 2 and 3). Using the independently tested models together with 54 global layers of soil, climate, biome and topography covariates (Supplementary Table 1), we digitally mapped I_{root}, I_{bulk} and their depth distribution (Methods, Extended Figs. 4 and 5) and their uncertainty across the globe at the resolution of 30 arc-second or approximately 1 km (Supplementary Figs. 6 and 7). Then, these I_{root} and I_{bulk} maps were used to estimate global I_{loss} (i.e., $I_{root} - I_{bulk}$, Fig. 4 and Extended Data Fig. 6) and its uncertainty (Methods, Extended Data Fig. 7). Across the globe, for each 1 km cell, I_{root} in the 0-200 cm soil profile ranges from 0.19 to 3.98 Mg ha^{-1} yr^{-1} (lower and upper limits of the 95% CI, Extended Data Fig. 4h). The maps reveal notable spatial patterns of I_{root}, with the highest I_{root} in tropical regions and lowest in Arctic regions. For I_{bulk}, it ranges from 0.15 to 2.58 Mg ha^{-1} yr^{-1} (Extended Data Fig. 5). I_{loss} ranges from –0.44 to 3.18 Mg ha^{-1} yr^{-1} across the globe (Fig. 4a). Higher I_{loss} generally occurs in lower latitudinal regions, and vice versa (Figs. 4a and c). In contrast, larger uncertainties in quantified I_{loss} generally occur in higher latitudes (Figs. 4b and d). These maps illustrate the global significance of direct C losses and provide spatial insights into prediction uncertainties.

Implications and conclusions

The connections and interactions between belowground and aboveground processes remain elusive and unquantified. One of the key issues is our poor understanding of the plant-soil interactions in which the rhizosphere may play a core mediating role[39]. Under elevated atmospheric CO_2, for example, numerous field manipulation experiments have found enhanced

194 photosynthetic C assimilation and thus stimulated C inputs to soil, but soil C stock shows no
195 or marginal response to such enhanced belowground C inputs and remains relatively stable[40,41].
196 The reason for this imbalance is widely debated. One explanation proposed is that microbial
197 decomposition of organic matter in bulk soil is accelerated as microbes "mine" nutrients from
198 soil organic matter in order to utilize the enhanced input of newly assimilated C, particularly
199 in nutrient-poor environments. But this ignores the fact that plants also need additional
200 nutrients to support their stimulated growth[4]. Our results shed light on another mechanism, i.e.,
201 only a minor fraction of additional I_{root} goes to bulk soil and the remaining majority has left the
202 system via direct loss pathways such as rhizosphere microbial respiration. Consistent with this
203 mechanism, a recent study of a mature forest under elevated CO_2 indeed found that half of the
204 extra C fixed under elevated CO_2 was quickly emitted through soil respiration, and did not
205 result in bulk soil C accumulation[41]. Our results indicate that it may be general across the globe
206 that the rhizosphere provides a buffer zone before environment change-induced plant responses
207 propagate into bulk soil. It is an open question how changes in plant communities and thus
208 their root systems under climate change[42,43] interact with rhizosphere C dynamics to influence
209 soil C turnover.

210 At the global scale, our results demonstrate that most root-derived C inputs to soil does
211 not directly contribute to the bulk soil C pool. That is, around 80% of root-derived C inputs
212 leaves the soil directly via various pathways potentially mediated by the rhizosphere. Here, we
213 propose three such pathways (Fig. 5). First, the majority of released C by roots as exudates
214 may be respired as CO_2 by microbes in the rhizosphere[24] instead of moving to the C pool in
215 bulk soil. Root-released C (in the form of exudates and root detritus) may mainly contribute to
216 the bulk soil C pool via by-products (e.g., necromass) of microbes which utilize root-derived
217 C in the rhizosphere. Indeed, there is evidence that microbial necromass accounts for >50% of
218 soil organic C in temperate cropping, grassland and forest topsoils[44]. Second, soil fauna feeds

on roots and microbes, and thus removes a fraction of root-derived C[23,45]. Third, root-derived C may pass directly to other systems beyond the soil layer such as bedrock or groundwater. For example, plant roots may penetrate to the bedrock[30], and thus the relevant root-derived C does not contribute to bulk soil C at all. It is also intriguing to note that the loss of root-derived C relative to inputs in each soil layer decreases with soil depth except the top 0-20 cm soil layer (Fig. 5). This may due to decreasing activities of soil microbes and fauna with soil depth; and in the top layer, bulk soil C inputs may include marked amount of C from soil surface[38].

Earth system models usually have a litter soil C pool with fast turnover rates[10,17], which may conceptually capture the direct C losses. However, the size and turnover rate of this pool have been rarely explicitly tested or verified. The spatially explicit maps for I_{root}, I_{bulk} and I_{loss} provide benchmark global layers to force and verify these models and explore the relevant implications for long-term C dynamics. The significant loss of root-derived C inputs provides insights into C sequestration by capturing the "leaked" C, such as through the application of biochar which can stabilize new root-derived C by formatting microaggregates via organo-mineral interactions[46]. We suggest that the oxidation of fixed C that occurs in the rhizosphere must be considered for reliable soil C predictions and land management to simulate C sequestration.

References

1 Jackson, R. B. *et al.* The ecology of soil carbon: Pools, vulnerabilities, and biotic and abiotic controls. *Annual Review of Ecology, Evolution, and Systematics* **48**, 419-445 (2017).

2 Regnier, P. *et al.* Anthropogenic perturbation of the carbon fluxes from land to ocean. *Nature Geoscience* **6**, 597-607 (2013).

3 Crowther, T. W. *et al.* Quantifying global soil carbon losses in response to warming. *Nature* **540**, 104-108 (2016).

4 Terrer, C. *et al.* Nitrogen and phosphorus constrain the CO_2 fertilization of global plant biomass. *Nature Climate Change* **9**, 684-689 (2019).

5 Luo, Z. K., Feng, W. T., Luo, Y. Q., Baldock, J. & Wang, E. L. Soil organic carbon dynamics jointly controlled by climate, carbon inputs, soil properties and soil carbon fractions. *Global Change Biology* **23**, 4430-4439 (2017).

6 Jobbágy, E. G. & Jackson, R. B. The vertical distribution of soil organic carbon and its relation to climate and vegetation. *Ecological Applications* **10**, 423-436 (2000).

7 Werth, M. & Kuzyakov, Y. C-13 fractionation at the root-microorganisms-soil interface: A review and outlook for partitioning studies. *Soil Biology Biochemistry* **42**, 1372-1384 (2010).

8 Balesdent, J. *et al.* Atmosphere–soil carbon transfer as a function of soil depth. *Nature* **559**, 599-602 (2018).

9 Hicks Pries, C. E., Castanha, C., Porras, R. C. & Torn, M. S. The whole-soil carbon flux in response to warming. *Science* **355**, 1420-1423 (2017).

10 He, Y. *et al.* Radiocarbon constraints imply reduced carbon uptake by soils during the 21st century. *Science* **353**, 1419-1424 (2016).

11 Luo, Y. *et al.* Toward more realistic projections of soil carbon dynamics by Earth system models. *Global Biogeochemical Cycles* **30**, 40-56 (2016).

12 Garnier, E. Resource capture, biomass allocation and growth in herbaceous plants. *Trends in Ecology & Evolution* **6**, 126-131 (1991).

13 Raich, J. W. & Nadelhoffer, K. J. Belowground carbon allocation in forest ecosystems: Global trends. *Ecology* **70**, 1346-1354 (1989).

14 Davidson, E. A. *et al.* Belowground carbon allocation in forests estimated from litterfall and IRGA-based soil respiration measurements. *Agricultural and Forest Meteorology* **113**, 39-51 (2002).

15 Luo, Z., Wang, G. & Wang, E. Global subsoil organic carbon turnover times dominantly controlled by soil properties rather than climate. *Nature Communications* **10**, 3688 (2019).

16 Fan, N. *et al.* Apparent ecosystem carbon turnover time: uncertainties and robust features. *Earth System Science Data Discuss* **2020**, 1-25 (2020).

17 Shi, Z. *et al.* The age distribution of global soil carbon inferred from radiocarbon measurements. *Nature Geoscience*, 555-559 (2020).

18 Sierra, C. A., Müller, M., Metzler, H., Manzoni, S. & Trumbore, S. E. The muddle of ages, turnover, transit, and residence times in the carbon cycle. *Global Change Biology* **23**, 1763-1773 (2017).

19 Carvalhais, N. *et al.* Global covariation of carbon turnover times with climate in terrestrial ecosystems. *Nature* **514**, 213-217 (2014).

20 Braakhekke, M. C. *et al.* The use of radiocarbon to constrain current and future soil organic matter turnover and transport in a temperate forest. *Journal Geophysical Research-Biogeosciences* **119**, 372-391 (2014).

21 Wu, D. *et al.* Accelerated terrestrial ecosystem carbon turnover and its drivers. *Global Change Biology* **20**, 5052-5062 (2020).

22 Massalha, H., Korenblum, E., Tholl, D. & Aharoni, A. Small molecules below-ground: the role of specialized metabolites in the rhizosphere. *Plant Journal* **90**, 788-807 (2017).

23 Osler, G. H. R. & Sommerkorn, M. Toward a complete soil C and N cycle: Incorporating the soil fauna. *Ecology* **88**, 1611-1621 (2007).

24 Finzi, A. C. *et al.* Rhizosphere processes are quantitatively important components of terrestrial carbon and nutrient cycles. *Global Change Biology* **21**, 2082-2094 (2015).

25 Drigo, B. *et al.* Shifting carbon flow from roots into associated microbial communities in response to elevated atmospheric CO_2. *Proc. Natl. Acad. Sci. U. S. A.* **107**, 10938-10942 (2010).

26 Kuzyakov, Y. & Razavi, B. S. Rhizosphere size and shape: Temporal dynamics and spatial stationarity. *Soil Biol. Biochem.* **135**, 343-360 (2019).

27 Schimel, J. P. & Schaeffer, S. M. Microbial control over carbon cycling in soil. *Front. Microbiol.* **3**, 11 (2012).

28 Strand, A. E., Pritchard, S. G., McCormack, M. L., Davis, M. A. & Oren, R. Irreconcilable differences: fine-root life spans and soil carbon persistence. *Science* **319**, 456-458 (2008).

29 Ledo, A. *et al.* Tree size and climatic water deficit control root to shoot ratio in individual trees globally. *New Phytol.* **217**, 8-11 (2018).

30 Canadell, J. *et al.* Maximum rooting depth of vegetation types at the global scale. *Oecologia* **108**, 583-595 (1996).

31 McCarthy, H. R. *et al.* Re-assessment of plant carbon dynamics at the Duke free-air CO_2 enrichment site: interactions of atmospheric CO_2 with nitrogen and water availability over stand development. *New Phytol.* **185**, 514-528 (2010).

32 Wieder, W. R., Cleveland, C. C., Smith, W. K. & Todd-Brown, K. Future productivity and carbon storage limited by terrestrial nutrient availability. *Nature Geoscience* **8**, 441-444 (2015).

33 Malhi, Y. *et al.* The variation of productivity and its allocation along a tropical elevation gradient: a whole carbon budget perspective. *New Phytol.* **214**, 1019-1032 (2017).

34 Lawrence, C. R. *et al.* An open-source database for the synthesis of soil radiocarbon data: International Soil Radiocarbon Database (ISRaD) version 1.0. *Earth Syst. Sci. Data* **12**, 61-76 (2020).

35 Negron-Juarez, R. I., Koven, C. D., Riley, W. J., Knox, R. G. & Chambers, J. Q. Observed allocations of productivity and biomass, and turnover times in tropical forests are not accurately represented in CMIP5 Earth system models. *Environmental Research Letters* **10** (2015).

318 36 Todd-Brown, K. E. O. *et al.* Causes of variation in soil carbon simulations from CMIP5
319 Earth system models and comparison with observations. *Biogeosciences* **10**, 1717-1736
320 (2013).
321 37 Bradford, M. A. *et al.* Managing uncertainty in soil carbon feedbacks to climate change.
322 *Nature Climate Change* **6**, 751-758 (2016).
323 38 Kaiser, K. & Kalbitz, K. Cycling downwards - dissolved organic matter in soils. *Soil Biol.*
324 *Biochem.* **52**, 29-32 (2012).
325 39 Haichar, F. E., Santaella, C., Heulin, T. & Achouak, W. Root exudates mediated
326 interactions belowground. *Soil Biol. Biochem.* **77**, 69-80 (2014).
327 40 Kuzyakov, Y., Horwath, W. R., Dorodnikov, M. & Blagodatskaya, E. Review and synthesis
328 of the effects of elevated atmospheric CO_2 on soil processes: No changes in pools, but
329 increased fluxes and accelerated cycles. *Soil Biology and Biochemistry* **128**, 66-78 (2019).
330 41 Jiang, M. *et al.* The fate of carbon in a mature forest under carbon dioxide enrichment.
331 *Nature* **580**, 227-231 (2020).
332 42 Lange, M. *et al.* Plant diversity increases soil microbial activity and soil carbon storage.
333 *Nature Communications* **6**, 8 (2015).
334 43 Sokol, N. W. & Bradford, M. A. Microbial formation of stable soil carbon is more efficient
335 from belowground than aboveground input. *Nature Geoscience* **12**, 46-53 (2019).
336 44 Liang, C., Amelung, W., Lehmann, J. & Kästner, M. Quantitative assessment of microbial
337 necromass contribution to soil organic matter. *Global Change Biology* **25**, 3578-3590
338 (2019).
339 45 van den Hoogen, J. *et al.* Soil nematode abundance and functional group composition at a
340 global scale. *Nature* **572**, 194-198 (2019).
341 46 Weng, Z. *et al.* Biochar built soil carbon over a decade by stabilizing rhizodeposits. *Nature*
342 *Climate Change* **7**, 371-376 (2017).

Methods

Soil profile data acquisition. Three datasets including net primary productivity (NPP) containing its belowground allocation (hereafter NPP_{data}), root biomass ($Root_{data}$) and soil radiocarbon measurement ($\Delta^{14}C_{data}$) from 725, 559 and 750 soil profiles, respectively, were used in this study. These measurement sites are distributed across the globe and cover the main biome types including tropical/subtropical forests, tropical/subtropical grasslands/savannas, temperate forests, temperate grasslands, Mediterranean/montane shrublands, boreal forests, tundra, deserts, and croplands (Extended Data Fig. 1). NPP_{data} is a comprehensive database of field observation of above- (ANPP) and belowground NPP (BNPP, i.e., root NPP), which was obtained through a thorough literature search and data synthesis from 54 published peer-reviewed papers (Supplementary references) and the ORNL DAAC NPP data collection (https://daac.ornl.gov/cgi-bin/dataset_lister.pl?p=13). Here we note that most NPP data only include root production but root exudates are difficult to measure and not included, which may result in underestimation of NPP, particularly BNPP.

$Root_{data}$ was compiled by Schenk and Jackson[47] (publicly obtainable from: https://daac.ornl.gov/cgi-bin/dsviewer.pl?ds_id=660). We calculated the depth distribution of root biomass in seven standard layers in the top 200 cm of soil profiles (i.e., 0-20, 20-40, 40-60, 60-80, 80-100, 100-150 and 150-200 cm), using the approach of Luo et al[15]. $\Delta^{14}C_{data}$ were obtained up to 7 July 2020 (ref.[34]). It is an open-source database for the synthesis of soil radiocarbon data using 'ISRaD.getdata' function in R packpage 'ISRaD'. From this dataset, the column 'lyr_14c_fill_extra' was used because it merges radiocarbon measurements reported as either $\Delta^{14}C$ or "fraction of modern" which was subsequently converted to $\Delta^{14}C$ (personal communication with the organizer of the dataset). We focused on the $\Delta^{14}C$ in mineral soils from 0 to 200 cm soil depth with clear records of observation year and soil layer (upper and lower depths). In total, we used 3,128 unique measurements of $\Delta^{14}C$ from 750 profiles

(Extended Data Fig. 1).

Estimation of root-derived C inputs to soil (I_{root}). Using the NPP_{data} dataset, belowground C allocation, i.e., root-derived C inputs to soil (I_{root}), can be directly estimated as belowground NPP (i.e., BNPP) recorded by NPP_{data} (Extended Data Fig. 1a). It is a significant challenge to determine the allocation of I_{root} to different soil layer depths using current technologies. However, it is reasonable to assume that I_{root} to a specific layer is proportional to root biomass in that layer. So we can infer C inputs to different soil layer depths by combining depth distribution of root biomass and BNPP[15]. The depth distribution of root biomass based on $Root_{data}$ (Extended Data Fig. 1) was used to estimate the depth distribution of I_{root}. In order to quantify the absolute I_{root} to each soil layer, ideally we need to know BNPP at the corresponding NPP_{data} location, but such data are unavailable for $Root_{data}$ sites. Here, we used a machine learning-based model for BNPP trained by NPP_{data} dataset to estimate I_{root} (i.e., BNPP) at $Root_{data}$ sites (see the section on **Machine learning models for I_{root} and I_{bulk}**), and then allocated I_{root} to seven standard layers (i.e., 0-20, 20-40, 40-60, 60-80, 80-100, 100-150 and 150-200 cm) using the depth distribution of root biomass recorded by $Root_{data}$ using the same approach as Luo et al[15]. At $\Delta^{14}C_{data}$ locations, we also used the model developed for BNPP at NPP_{data} sites to predict I_{root}, which is further allocated to different soil layers according to the vertical distribution of I_{bulk}, assuming these two variables (i.e., depth distribution predicted by $Root_{data}$ and $\Delta^{14}C_{data}$) follow a similar pattern of depth distribution (Fig. 1d, see the section on **Machine learning models for I_{root} and I_{bulk}**).

Estimation of actual C inputs to bulk soil (I_{bulk}). Under the assumption of steady state, C inputs to bulk soil (I_{bulk}) can be estimated as bulk soil C stock divided by C age. Using the $\Delta^{14}C_{data}$, a soil radiocarbon model[48] was adopted to estimate C_{age}:

$$\frac{dA^{soil}}{dt} = k \cdot A^{input} - (k + \gamma) \cdot A^{soil}, \quad (1)$$

where A^{input} is the $^{14}C/^{12}C$ ratio of C inputs into bulk soil and assumed to be equal to the $^{14}C/^{12}C$ ratio of the atmosphere, A^{soil} is the $^{14}C/^{12}C$ ratio of bulk soil C, k is the decay rate of bulk soil C, and γ is the β-decay rate of ^{14}C and equal to 1/8267 per year. Before the nuclear testing in the 1950s and 1960s, atmospheric $^{14}C/^{12}C$ ratio was relatively stable. Under the steady state assumption, A^{soil} can be estimated by Equation (2), and with A^{soil} measurements at the steady state, k can be estimated by Equation (3) as follow:

$$A^{soil} = \frac{k}{k+\gamma} \cdot A^{input}, \quad (2)$$

$$k = \gamma \cdot \frac{A^{soil}}{A^{input} - A^{soil}}. \quad (3)$$

If A^{soil} is measured after the nuclear testing, Equation (3) cannot be directly used to estimate k because the atmospheric $^{14}C/^{12}C$ ratio is significantly increased. However, the estimated A^{soil} by Equation (3) provides a starting point as the pre-nuclear test status. Combining Equations (3) and (2), we can start the modelling from any pre-nuclear test time (from 1950 in this study), and estimate k using time-series measurements of A^{input} (i.e., the ^{14}C activity of the atmosphere in each year after the nuclear testing) and A^{soil} measurements at any time points after the testing. Once k is obtained, the reciprocal of the decay rate k defines C_{age}. Atmospheric radiocarbon data for each year during the period 1950-2010 were extracted from Hua et al[49] for the northern and southern hemispheres, separately (Supplementary Fig. 5a). To utilise the soil radiocarbon measurements conducted in more recent years, we interpolated the atmospheric radiocarbon data during the period of 2011-2019 using random forest imputation method in the 'mice' function in R 3.6.1 (ref.[50]). In these databases, however, radiocarbon data are reported as $\Delta^{14}C$ – the per mille (‰) deviation from a standard of fixed isotopic composition:

$$\Delta^{14}C = \left(\frac{A^{sample}}{A^{standard}} - 1\right) \cdot 1000. \quad (4)$$

where A^{sample} and $A^{standard}$ are the $^{14}C/^{12}C$ ratio of measured samples and a common international standard respectively. Hence, we can estimate A^{input} and A^{soil} based on the corresponding reported $\Delta^{14}C$ as:

$$A^{sample} = \left(\frac{\Delta^{14}C}{1000} + 1\right) \cdot A^{standard}. \quad (5)$$

Replacing A^{input} and A^{soil} in Equations (2-4) with Equation (5), we find that the model is independent of $A^{standard}$, enabling us to calculate k thus C_{age} (i.e., $1/k$) using $\Delta^{14}C$ in the bulk soil and atmosphere. Finally, I_{bulk} is estimated as:

$$I_{bulk} = \frac{C_{stock}}{C_{age}}. \quad (6)$$

where C_{stock} is the soil C stock in a typical layer for which $\Delta^{14}C$ is recorded. For $\Delta^{14}C_{data}$ soil profiles soil C stock is not recorded, we retrieved C stock from the WISE30sec database[51] using the coordinates of the soil measurement locations. Using this approach, a total of 3,128 estimates of I_{bulk} in different soil layer depths across 750 soil profiles were obtained. To facilitate the comparison with I_{root} at standard soil layers, we harmonized I_{bulk} at the $\Delta^{14}C_{data}$ profiles to above-mentioned seven layers (i.e., 0-20, 20-40, 40-60, 60-80, 80-100, 100-150 and 150-200 cm) using a machine learning model, which on average explained 95% of the variation of I_{bulk} in different soil depths for the $\Delta^{14}C_{data}$ profiles (Supplementary Fig. 8f, see the section on **Machine learning models for I_{root} and I_{bulk}**).

Estimation of direct loss of root-derived C inputs (I_{loss}). Direct C losses of root-derived C inputs (I_{loss}, i.e., root-derived C that does not enter bulk soil C pool) can be inferred as the difference between I_{root} and I_{bulk} (i.e., $I_{root} - I_{bulk}$). However, I_{root} and I_{bulk} cannot be simultaneously and directly determined using observed data at the sites of the NPP_{data}, $Root_{data}$, or $\Delta^{14}C_{data}$ data sets. We needed to predict I_{bulk} at NPP_{data} and $Root_{data}$ sites and also predict I_{root}

436 at $\Delta^{14}C_{data}$ and $Root_{data}$ sites (Extended Data Table 1). We integrated NPP_{data}, $\Delta^{14}C_{data}$ and
437 $Root_{data}$ datasets to estimate I_{loss} at sites in each dataset and conducted cross-comparisons to
438 verify I_{loss} estimations as well as quantify uncertainties in I_{loss} based on different datasets
439 (Extended Data Table 1).

440 At sites for each dataset, we estimated I_{root} and I_{bulk} using the observed data as a priority.
441 If the observed data were unavailable, we used machine learning-based statistical models (see
442 the section on **Machine learning models for I_{root} and I_{bulk}**) to predict the missing values. Each
443 estimation of I_{loss} utilized at least one observed dataset (Extended Data Table 1). As a
444 comparison to BNPP estimation based on NPP_{data}, additionally we included the MODIS NPP[52]
445 in our estimation of I_{loss}. Specifically, we retrieved NPP data from the MODIS NPP product
446 using the geographical coordinates of each site location for the three observed datasets. To
447 determine the quantity of MODIS NPP allocated belowground (i.e., BNPP), we additionally fit
448 a machine learning-based regression model of f_{BNPP} (i.e., BNPP/NPP) using the observed NPP
449 and BNPP at NPP_{data} locations (see the section on **Machine learning models for I_{root} and**
450 **I_{bulk}**). In this way, we obtained six independent estimations of I_{loss} (Extended Data Table 1),
451 which enabled us to make cross-comparisons and assess uncertainties in I_{loss}. Details of the
452 quantifications of each I_{loss} estimate are provided in Extended Data Table 1.

453 Here, it should be noted that the observed NPP is somewhat inconsistent with MODIS
454 NPP for the NPP_{data} sites (Extended Data Fig. 8). In all biomes assessed, on average MODIS
455 NPP is an underestimation of field observed NPP_{data} (Extended Data Fig. 8b). This
456 phenomenon may result from the mismatch of spatiotemporal scales of the two datasets. That
457 is, MODIS NPP represents the annual average of a ~1 km^2 pixel, while NPP_{data} is measured at
458 a specific location and time. Further, MODIS NPP has uncertainties[53].

459 **Drivers of I_{root} and I_{bulk}.** We used linear mixed regression to examine the relationship of a

suite of predicting variables with I_{root} and I_{bulk}. We assume I_{root} is associated with soil properties (i.e., 20 soil physiochemical properties), climatic factors (i.e., 19 bioclimatic variables), topographic conditions (i.e., 13 topographical variables; Supplementary Table 1). Here we only considered the whole-profile I_{root} due to data availability. For I_{bulk}, however, apart from these predictor variables, soil layer including top and bottom depths were also included as driving factors. For both I_{root} and I_{bulk}, biome type was treated as a random effect, that is, the coefficients of other predictor variables vary among biome types. The multivariate linear mixed-effects model is expressed as[54]:

$$y_i = N\left(X_i\beta, \sigma_y^2\right), for\ i = 1, \ldots . n, \quad (7)$$

and β is further modelled within each biome type:

$$\beta_j = N(\mu_\alpha, \sigma_\alpha^2), \text{for } j = \text{each of the 9 biome types}, \quad (8)$$

where n is the sample size of I_{root} and I_{bulk}, respectively, y_i the ^{i}th variable of interest (i.e., I_{root} and I_{bulk}), X_i the vector of predictor variables; β a vector of coefficients for the predictor variables; μ_α the estimation of β; σ_y^2 and σ_α^2 the error terms for y_i and β_j, respectively, which follow a normal distribution (N). Before fitting the linear mixed-effects regression, all variables were standardized to unit variance therefore the absolute magnitude of the coefficients for the predictor variables reflect their relative importance[54]. A principal component analysis (PCA) was applied to eliminate potential correlations in the 20 edaphic variables, 19 climatic variables and 13 topographic variables, respectively. The most important PCs with variances greater than 1 were retained for the regression[55]. The PCA and linear mixed-effect model regression were conducted using the 'procomp' function in the 'stats' package and the 'lmer' function in the 'arm' package, respectively, in R 3.6.1 (ref.[50]).

Environmental covariates. We obtained 54 global layers of soil, climate, topography and biome type. A total of 20 soil physical and chemical properties was obtained from ISRIC-WISE

soil profile database[51] with a spatial resolution of 1 km. We obtained 19 climatic attributes with the same resolution as the WISE database from WorldClim[56], which quantifies biologically meaningful variables using monthly temperature and precipitation. In addition, we derived spatial layers of biome type using the approach of Luo et al[15]. Specifically, we aggregated two land cover maps (i.e., the MODIS land cover map[57] and the Terrestrial Ecoregions of the World[58]) to generate a map consisting of nine biome types. We also retrieved the soil order data from Global Soil Regions Map database (https://www.nrcs.usda.gov/wps/portal/nrcs/detail/soils/use/?cid=nrcs142p2_054013). Finally, we calculated 13 topographic attributes from SRTM-DEM at 90 m resolution (http://srtm.csi.cgiar.org) using 'elevatr', 'spatialEco' and 'dynatopmodel' packages in R 3.6.1 (ref.[50]) and SAGA[59]. More details of these global spatial covariate layers are given in Supplementary Table 1.

Machine learning models for predicting I_{root} and I_{bulk}. To extrapolate I_{root} and I_{bulk} spatially, we generated spatial predictive models of these two variables, by treating the edaphic, climatic, topographic attributes, and biome type (i.e., the 54 global layers of environmental covariates) as potential drivers (Supplementary Table 1). Using the geographical coordinates of NPP_{data} and $\Delta^{14}C_{data}$ locations, we retrieved the above-mentioned environmental covariates. For the I_{bulk} model, the radiocarbon-derived I_{bulk} of the 3,128 soil radiocarbon measurements was treated as a dependent variable. For I_{bulk}, soil layers (the top and bottom depths of a layer) were also included as predictors. Using the model for I_{bulk}, we quantified I_{bulk} at NPP_{data} and $Root_{data}$ sites and at the global scale (Extended Data Fig. 5). Because soil layers were treated as independent drivers in the model of I_{bulk}, we could directly predict the depth distribution of I_{bulk}. It is also important to highlight that the depth distribution of I_{bulk} is comparable with that of root biomass (Fig. 1d). This gave us confidence to use I_{bulk} depth distribution to infer I_{root} depth distribution, where this information was unavailable (e.g., at NPP_{data} and $\Delta^{14}C_{data}$ locations).

Treating the observed BNPP (i.e., I_{root}) and f_{BNPP} (the fraction of BNPP to total NPP) data at the NPP_{data} sites as dependent variables, we fitted two machine learning-based models for I_{root} and f_{BNPP}, respectively. The purpose of fitting the model for f_{BNPP} is to estimate the allocation of the NPP retrieved from the MODIS NPP product to belowground, and further calculate I_{root} derived from MODIS NPP (Extended Data Table 1). Here, the 52 environmental covariates (Supplementary Table 1) at the NPP_{data} sites were used as independent variables. For all these three models (i.e., I_{bulk}, I_{root} and f_{BNPP}), we trained a suite of machine learning algorithms including random forest (RF), extreme gradient boosting (XGBoost), Cubist, support vector machines (SVM) and multivariate adaptive regression splines (MARS). Before fitting these machine learning models, we first converted the categorical variables (e.g., biome type) to dummy variables. Then, the function 'findCorrelation' and 'findLinearCombo' in R package 'caret' was used to exclude those attributes with high multicollinearities. The remaining variables were further used in model calibration (80% stratified samples) and validation (the remaining 20% stratified samples). It should be noted that, when fitting the model for I_{bulk} used to harmonize I_{bulk} at the $\Delta^{14}C_{data}$ profiles to the seven standard soil layers, all the I_{bulk} data were used to constrain the model (Supplementary Fig. 8). We also generated an ensemble model using a regression method of principal component analysis (PCA) with R packages 'pls' and 'caret' based on the prediction outputs from the top three models with the lowest RMSE (rooted mean squared error). Specifically, the better an individual model's performance is (with a smaller root mean squared error), the more the model's output contributes to the ensemble model's final predictions. The results showed that the ensemble model and random forest model can generally better simulate I_{root} (Extended Data Fig. 2), I_{bulk} (Extended Data Fig. 3) and f_{BNPP} (Extended Data Fig. 9) compared with other four algorithms (i.e., XGBoost, SVM, Cubist and MARS). Using these fitted machine learning models (ensemble models) and retrieving the predicting variables at other locations, we predicted I_{bulk}

at $Root_{data}$ and NPP_{data} sites, and also calculated I_{root} and f_{BNPP} at $Root_{data}$ and $\Delta^{14}C_{data}$ locations.

Global mapping and prediction uncertainty. Using the fitted machine learning models, we mapped I_{root} (Extended Data Fig. 4), I_{bulk} (Extended Data Fig. 5) and I_{loss} (i.e., $I_{root} - I_{bulk}$, Extended Data Fig. 6) in the seven standard layers across the globe at the resolution of 30 arc-second (~1 km) grid. Here, we used the random forest model, rather than the ensemble model, due mainly to limited computing resources and the overall strong performance of RF models compared to model ensembles (Extended Data Figs. 2, 3 and 9).

In each grid, the model was run using environmental covariates extracted from the global data layers. Prediction uncertainty was quantified using a Monte Carlo approach proposed for digital soil mapping with machine learning by Viscarra Rossel et al[60] and Coulston et al[61]. First, 500 bootstrap samples of soil profiles were randomly drawn with replacement to construct 500 random forest models. For each bootstrap resample, 80% of the soil profile-specific data (randomly selected without replacement) were used to train a random forest model with 500 individual trees, while the other 20% were reserved for model testing. For each derived random forest model, a scaling factor τ for each observation in the hold-out testing data was estimated to approximate prediction uncertainty[61]:

$$\tau = \sqrt{\frac{\left(y - \bar{\hat{y}}\right)^2}{var(\hat{y})}}, \quad (9)$$

where y is the observed value, $var(\hat{y})$ the variance of the predictions of individual trees (i.e., 500 trees) in the random forest model, $\bar{\hat{y}}$ the average of $\hat{y}$, i.e., the prediction of the random forest model. As such, we obtained a vector of τ with length equal to the number of observations in the hold-out data multiplied by bootstrapping 500 times, which represents the distribution of model prediction errors. Finally, a new random forest model based on all available data was trained for mapping. For mapping in each grid, a variable of interest θ (e.g.,

I_{bulk}) was estimated as:

$$\theta = \bar{\hat{y}} \pm \hat{\tau} \cdot sd(\hat{y}), \quad (10)$$

where $\bar{\hat{y}}$ is the prediction of the new random forest model, $sd(\hat{y})$ the standard deviation of the predictions of individual trees in the new random forest model, $\hat{\tau}$ the scaling factor for desired prediction interval width estimated based on the derived distribution of model prediction errors. Using a Monte Carlo approach, we took the 95th percentile of the distribution as $\widehat{\tau_{95}}$to quantify the 95% prediction interval[61]. In each grid, uncertainty of I_{root} and I_{bulk} was standardized as the absolute value of corrected margin of the deviation [i.e., $\widehat{\tau_{95}} \cdot sd(\hat{y})$] divided by the mean (i.e., $\bar{\hat{y}}$). I_{loss} for each grid was estimated by $I_{root} - I_{bulk}$ with their uncertainties propagated by conducting 500 Monte Carlo simulations. The median and average of I_{loss} were estimated based on the 500 simulations, and the uncertainty of I_{loss} was estimated as the margin of deviation of the 500 simulations divided by their mean.

Data and code availability

All data supporting the findings of this study are available on https://figshare.com/articles/dataset/Datasets_of_NPP_soil_radiocarbon_and_root_biomass/12840050. Code used to generate the results is available from the corresponding author (luozk@zju.edu.cn).

Refereces

47 Jochen, S. H. & B., J. R. The global biogeography of roots. *Ecological Monographs* **72**, 311-328 (2002).

48 Cherkinsky, A. & Brovkin, V. Dynamics of radiocarbon in soils. *Radiocarbon* **35**, 363-367 (1993).

49 Hua, Q., Barbetti, M. & Rakowski, A. Z. Atmospheric radiocarbon for the period 1950–2010. *Radiocarbon* **55**, 2059-2072 (2013).

50 R: A language and environment for statistical computing. R Foundation for Statistical Computing, Vienna, Austria, (2020).

51 Batjes, N. H. Harmonized soil property values for broad-scale modelling (WISE30sec) with estimates of global soil carbon stocks. *Geoderma* **269**, 61-68 (2016).

52 Zhao, M. & Running, S. W. Drought-induced reduction in global terrestrial net primary production from 2000 through 2009. *Science* **329**, 940-943 (2010).

53 Zhao, M., Heinsch, F. A., Nemani, R. R. & Running, S. W. Improvements of the MODIS terrestrial gross and net primary production global data set. *Remote Sensing of Environment* **95**, 164-176 (2005).

54 Gelman, A. & Hill, J. *Data analysis using regression and multilevel/hierarchical models*. (Cambridge University Press, 2006).

55 Kaiser, H. F. The application of electronic computers to factor analysis. *Educational and Psychological Measurement* **20**, 141-151 (1960).

56 Fick, S. E. & Hijmans, R. J. WorldClim 2: new 1 - km spatial resolution climate surfaces for global land areas. *International Journal of Climatology* (2017).

57 Channan, S., Collins, K. & Emanuel, W. Global mosaics of the standard MODIS land cover type data. *University of Maryland and the Pacific Northwest National Laboratory, College Park, Maryland, USA* **30** (2014).

58 Olson, D. M. *et al.* Terrestrial ecoregions of the world: a new map of life on earth: A new global map of terrestrial ecoregions provides an innovative tool for conserving biodiversity. *Bioscience* **51**, 933-938 (2001).

59 Conrad, O. *et al.* System for automated geoscientific analyses (SAGA) v. 2.1.4. *Geosci. Model Dev.* **8**, 1991-2007 (2015).

60 Viscarra Rossel, R. A., Webster, R., Bui, E. N. & Baldock, J. A. Baseline map of organic carbon in Australian soil to support national carbon accounting and monitoring under climate change. *Global Change Biology* **20**, 2953-2970 (2014).

61 Coulston, J. W., Blinn, C. E., Thomas, V. A. & Wynne, R. H. Approximating prediction uncertainty for random forest regression models. *Photogrammetric Engineering & Remote Sensing* **82**, 189-197 (2016).

Authors contributions Z.L. conceived the study; G.W., S.C., Z.L. compiled the data; G.W., L.X. and Z.L. led the data assessment with the contributions of X.M., X.G., S.Z. and M.W. ; L.X. conducted global mapping; G.W. and Z.L. interpreted the results with the contribution of A.C., G.Z., Z.S., S.Z and M.W.; Z.L. led manuscript writing with substantial contributions of G.W. and A.C.

Competing interests The authors declare no competing interests.

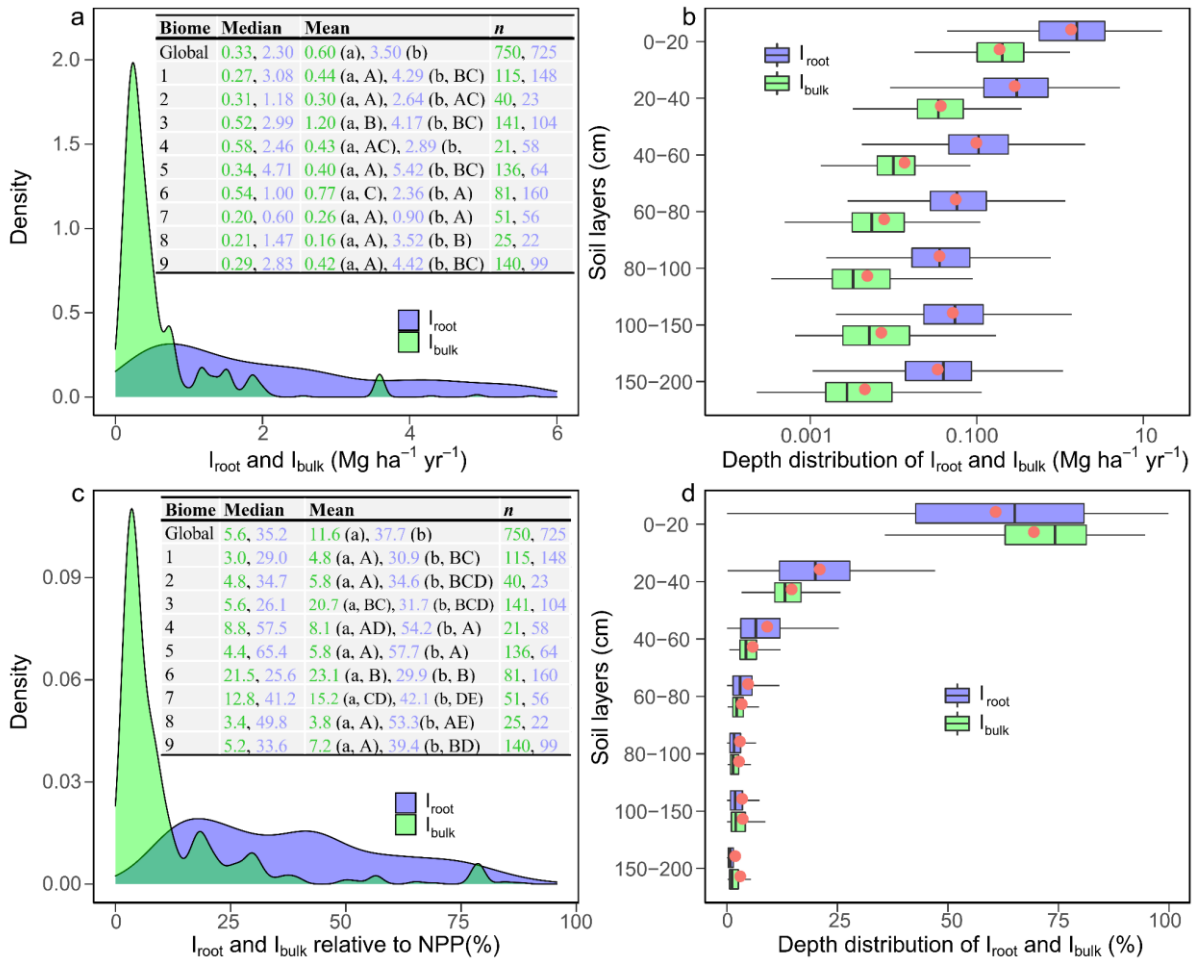

616

617 **Fig. 1. Root-derived carbon inputs (I_{root}) and actual carbon inputs to bulk soil (I_{bulk}). a**:
618 the probability density distribution of I_{root} (blue color) and I_{bulk} (green color); **b**: the depth
619 distribution of I_{root} and I_{bulk}; **c**: the probability density distribution of the percentage fraction of
620 I_{root} and I_{bulk} relative to net primary production (NPP); **d**: the percentage depth distribution of
621 I_{root} and I_{bulk} relative to total I_{root} and I_{bulk}, respectively. Inset tables in **a** and **c** show the median,
622 mean and sample size across the globe and in nine biome types (1: tropical/subtropical forests,
623 2: tropical/subtropical grasslands/savannas, 3: temperate forests, 4: temperate grasslands, 5:
624 Mediterranean/montane shrublands, 6: boreal forests, 7: tundra, 8: deserts, and 9: croplands),
625 and different lowercase and capital letters indicate significant ($P < 0.05$) difference between
626 I_{root} and I_{bulk} and between biomes, respectively. Boxplots (**b** and **d**) show the median and
627 interquartile range with whiskers extending to 1.5 times of the interquartile range, and red dots
628 show averages.

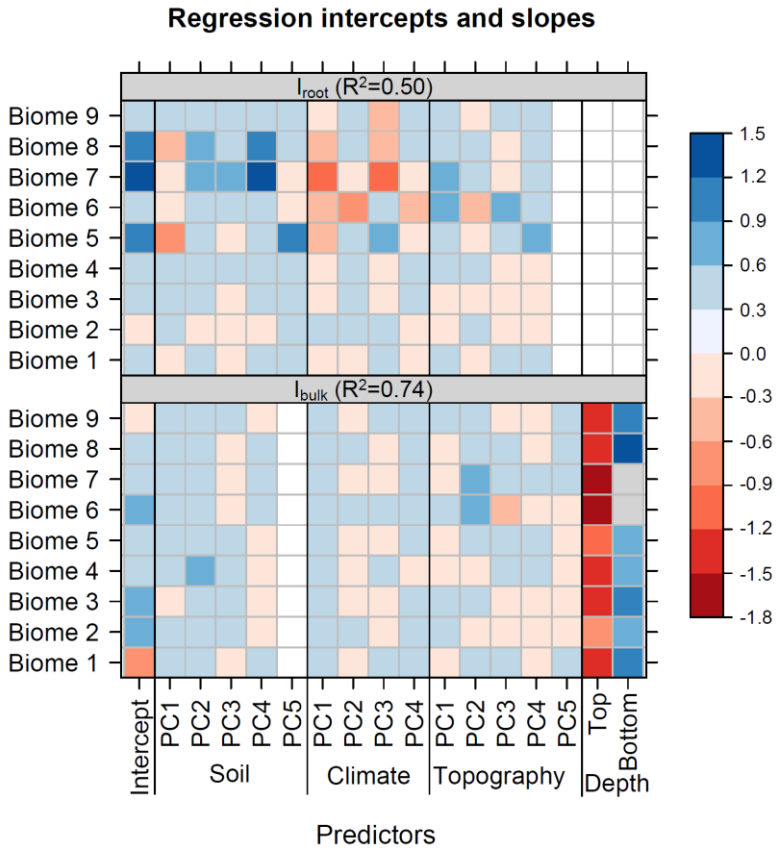

629

630 **Fig. 2. Drivers of root derived carbon input (I_{root}) and actual carbon input to bulk soil**
631 **(I_{bulk}).** Color grids show the coefficients and intercepts of linear mixed-effect regression
632 models for I_{root} (up panel) and I_{bulk} (bottom panel) treating biome type as a random effect. Blank
633 grids indicate that the predictor variable was not included; grey grids indicate that the effect is
634 insignificant (i.e., p>0.05). Biome 1-9 show the nine biome types (1: tropical/subtropical
635 forests, 2: tropical/subtropical grasslands/savannas, 3: temperate forests, 4: temperate
636 grasslands, 5: Mediterranean/montane shrublands, 6: boreal forests, 7: tundra, 8: deserts, and
637 9: croplands). PC1-5 are the most important principal components (PCs) of different groups of
638 driving factors (i.e., soil, climate, topography and depth). Top and Bottom show the top and
639 bottom depths of soil layer, which are treated as driving factors for I_{bulk}. The R^2 for the models
640 of I_{root} and I_{bulk} are 0.50 and 0.74, respectively. Detailed principal component analyses on the
641 predictor variables are presented in Supplementary Figs. 3 and Fig. 4.

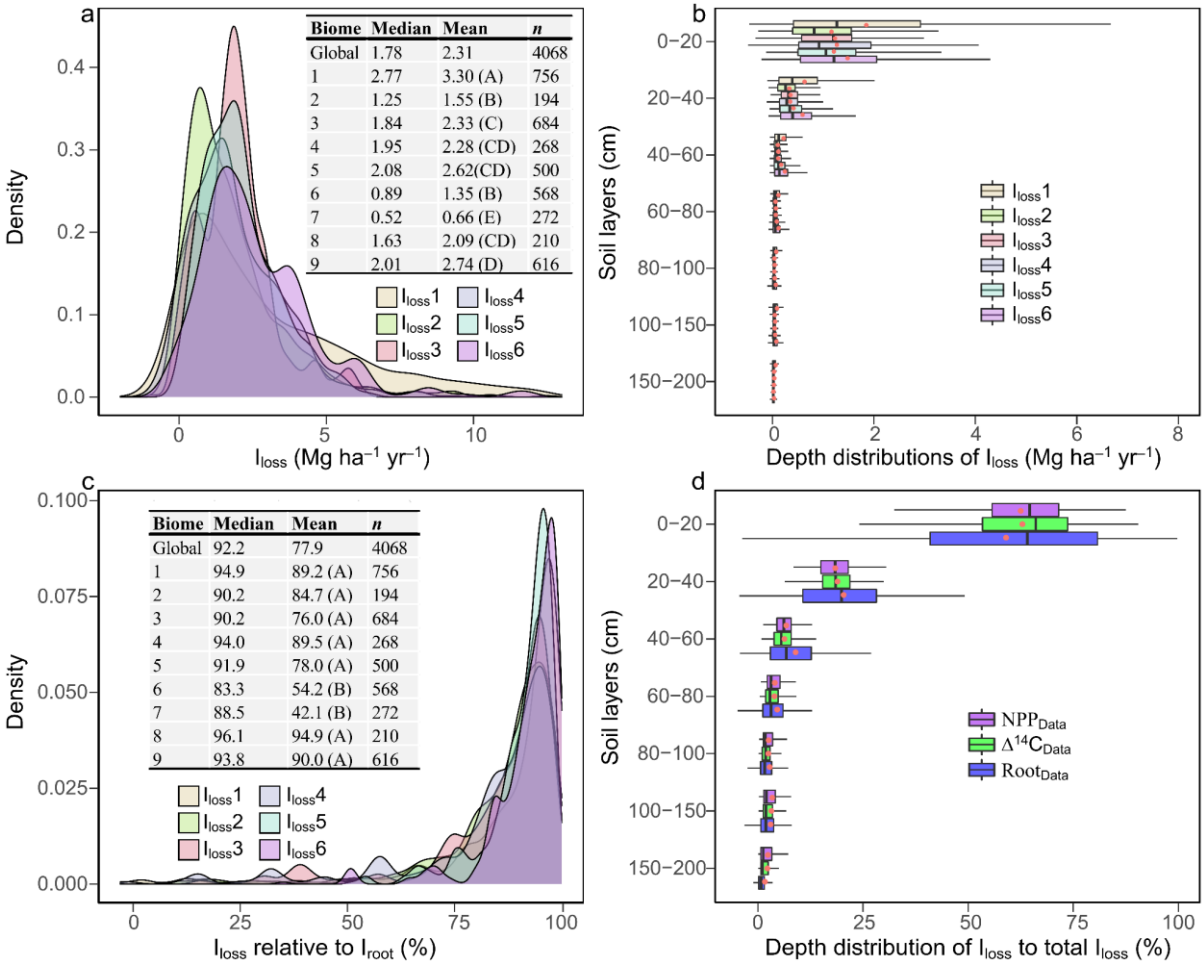

642

643 **Fig. 3. Direct soil carbon loss (I_{loss}, which is estimated as $I_{root} - I_{bulk}$) without contributing**
644 **to bulk soil carbon pool. a**, the probability density distribution of I_{loss} quantified using six
645 independent data sources and/or methods (I_{loss}1-6), which are described in Extended Data Table
646 1; **b**, depth distribution of I_{loss}; **c**, the probability density distribution of the percentage fraction
647 of I_{loss} relative to I_{root}; **d**, the percentage I_{loss} in each soil layer relative to total I_{loss}. Inset tables
648 in **a** and **c** show the median, mean and sample size across the globe and in nine biome types.
649 Different capital letters indicate significant ($P < 0.05$) difference between biomes. See Fig. 1
650 for details of the 9 biome types. Boxplots (**b** and **d**) show the median and interquartile range
651 with whiskers extending to 1.5 times of interquartile range, and red dots show averages

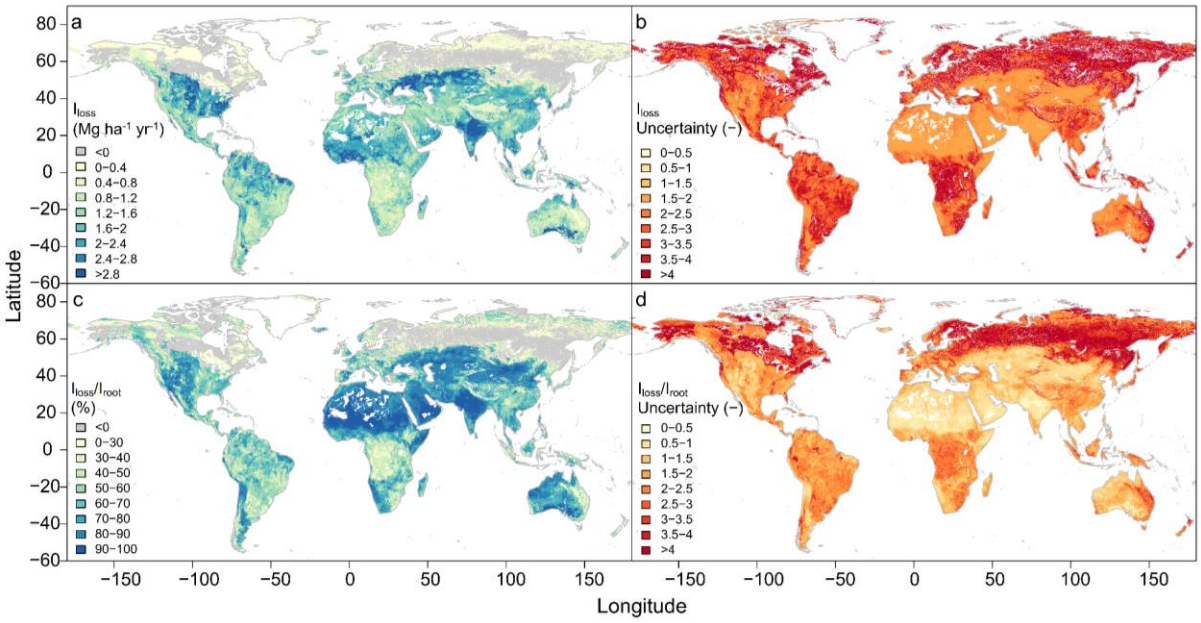

652

653 **Fig. 4. Global pattern of direct soil carbon loss (i.e., I_{loss}) in the 0-200 cm soil profile. a**,
654 I_{loss}; **b**, uncertainty of I_{loss} [in terms of the margin of the deviation of 500 Monte Carlo
655 simulations divided by their mean, taking into account uncertainties in both observational data
656 sets and prediction models]; **c**, the proportion of I_{loss} relative to root-derived C inputs (I_{root}); **d**,
657 uncertainty of the proportion of I_{loss} relative to I_{root}.

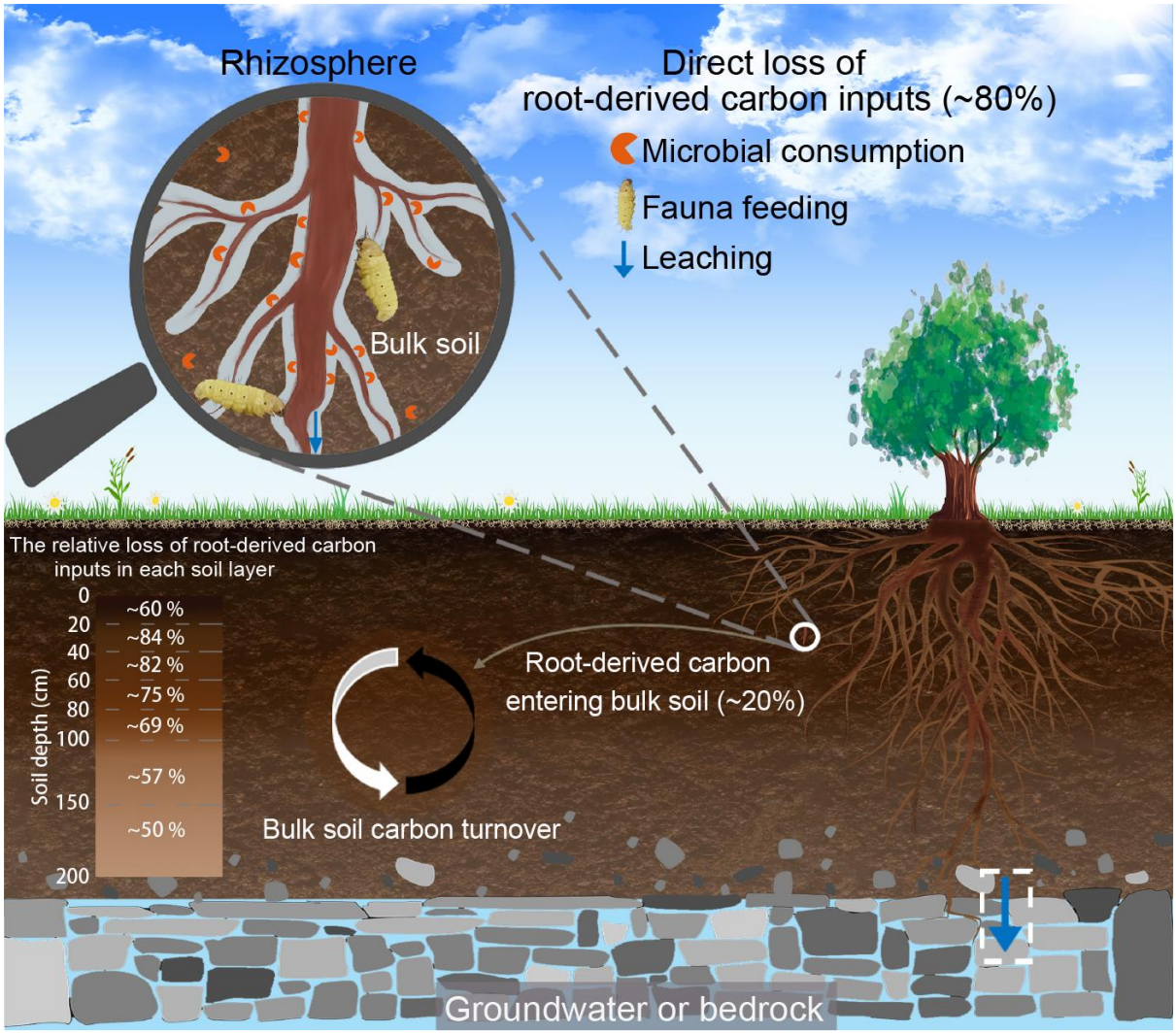

Fig. 5. Schematic representation of fluxes of root-derived carbon inputs. The majority of root-derived carbon inputs is lost directly via three potential pathways: rhizosphere microbial consumption, fauna feeding and leaching; and does not contribute to bulk soil carbon pool.

Extended Data Table 1. Estimation of root-derived carbon inputs (I_{root}), carbon inputs to bulk soil (I_{bulk}) and direct carbon loss of I_{root} (I_{loss}=I_{root}-I_{bulk}) in soil profiles at NPP_{data}, $\Delta^{14}C_{data}$ and $Root_{data}$ sites, respectively. BNPP is the belowground net primary production (NPP), f_{BNPP} is the fraction of BNPP to NPP.

Sites	Variables to calculate I_{root}	I_{root} (Mg ha^{-1} yr^{-1})	I_{bulk} (Mg ha^{-1} yr^{-1})	I_{loss} (Mg ha^{-1} yr^{-1})
NPP_{data}	①^{OBS}: observed BNPP ②^{PRE}: predicted BNPP depth distribution using $\Delta^{14}C_{data}$-derived models ③^{MOD}: MODIS NPP ④^{OBS}: observed f_{BNPP}	❶=①^{OBS}×②^{PRE} ❷=③^{MOD}×④^{OBS}×②^{PRE}	①^{PRE}: predicted using $\Delta^{14}C_{data}$-derived models	❶–①^{PRE} (I_{loss}1) ❷–①^{PRE} (I_{loss}2)
$\Delta^{14}C_{data}$	⑤^{PRE}: predicted BNPP using NPP_{data}-derived models ⑥^{OBS}: observed BNPP depth distribution ⑦^{MOD}: MODIS NPP ⑧^{PRE}: predicted f_{BNPP} using NPP_{data}-derived models	❸=⑤^{PRE}×⑥^{OBS} ❹=⑦^{MOD}×⑧^{PRE}×⑥^{OBS}	②^{OBS}: observed	❸–②^{OBS} (I_{loss}3) ❹–②^{OBS} (I_{loss}4)
$Root_{data}$	⑨^{PRE}: predicted BNPP using NPP_{data}-derived models ⑩^{OBS}: observed BNPP depth distribution ⑪^{MOD}: MODIS NPP ⑫^{PRE}: predicted f_{BNPP} using NPP_{data}-derived models	❺=⑨^{PRE}×⑩^{OBS} ❻=⑪^{MOD}×⑫^{PRE}×⑩^{OBS}	③^{PRE}: predicted using $\Delta^{14}C_{data}$-derived models	❺–③^{PRE} (I_{loss}5) ❻–③^{PRE} (I_{loss}6)

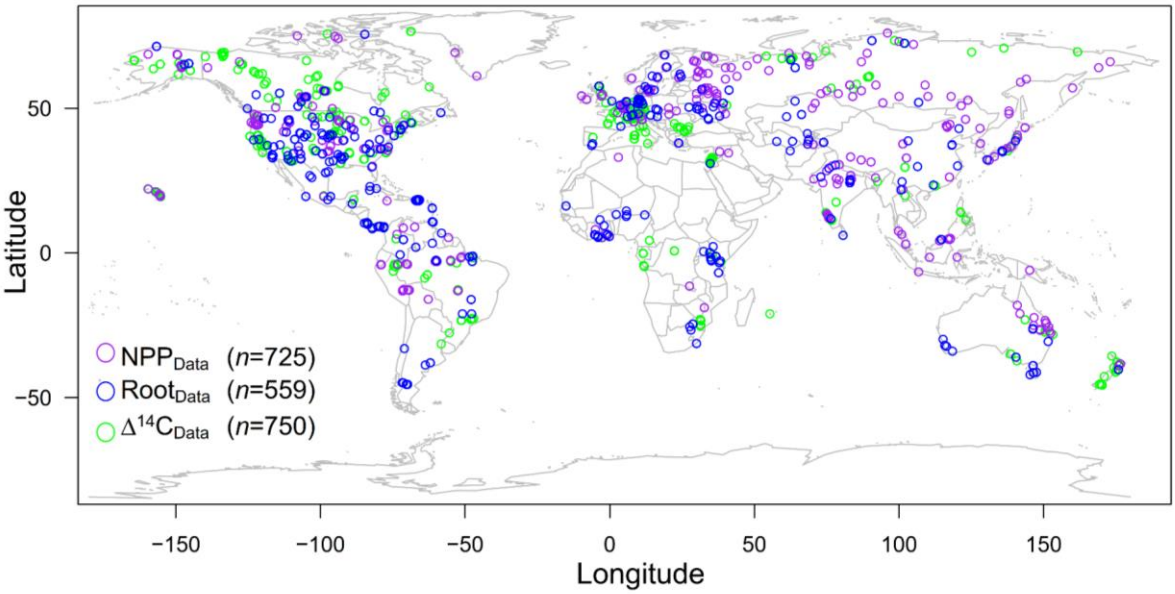

667

668 **Extended Data Fig. 1. Location distribution of measurements of above- and belowground**
669 **NPP (NPP_{data}), root biomass distribution ($Root_{data}$) and soil radiocarbon content**
670 **($\Delta^{14}C_{Data}$).** Values in parentheses show the number of profiles for each of the three data sets.

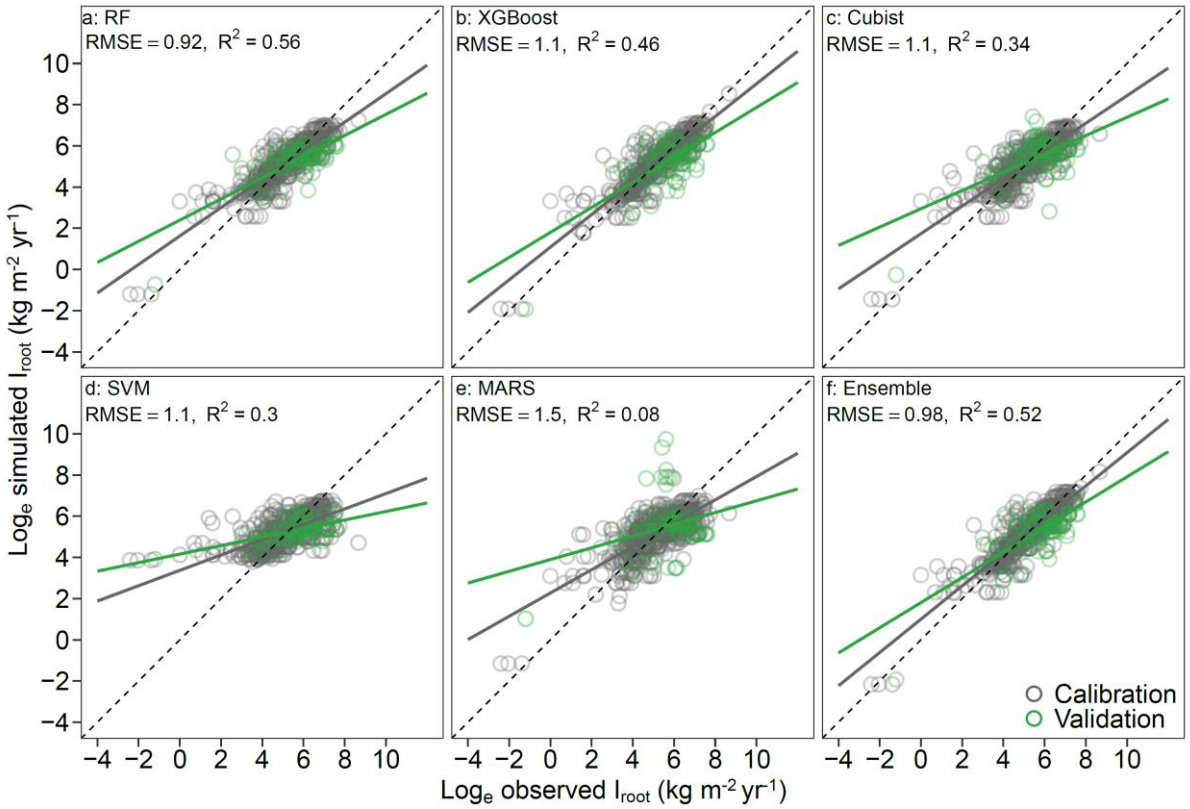

671

672 **Extended Data Fig. 2. Performance of fitted machine learning models to predict I_{root}.** Data
673 are log-transformed. **a**, random forest (RF); **b**, extreme gradient boosting (XGBoost); **c**, Cubist;
674 **d**, support vector machines (SVM); **e**, multivariate adaptive regression splines (MARS); **f**, the
675 ensemble model of **a-e**. For each individual model, 80% of the stratified samples of
676 observations were used for model calibration, with the other 20% for validation.

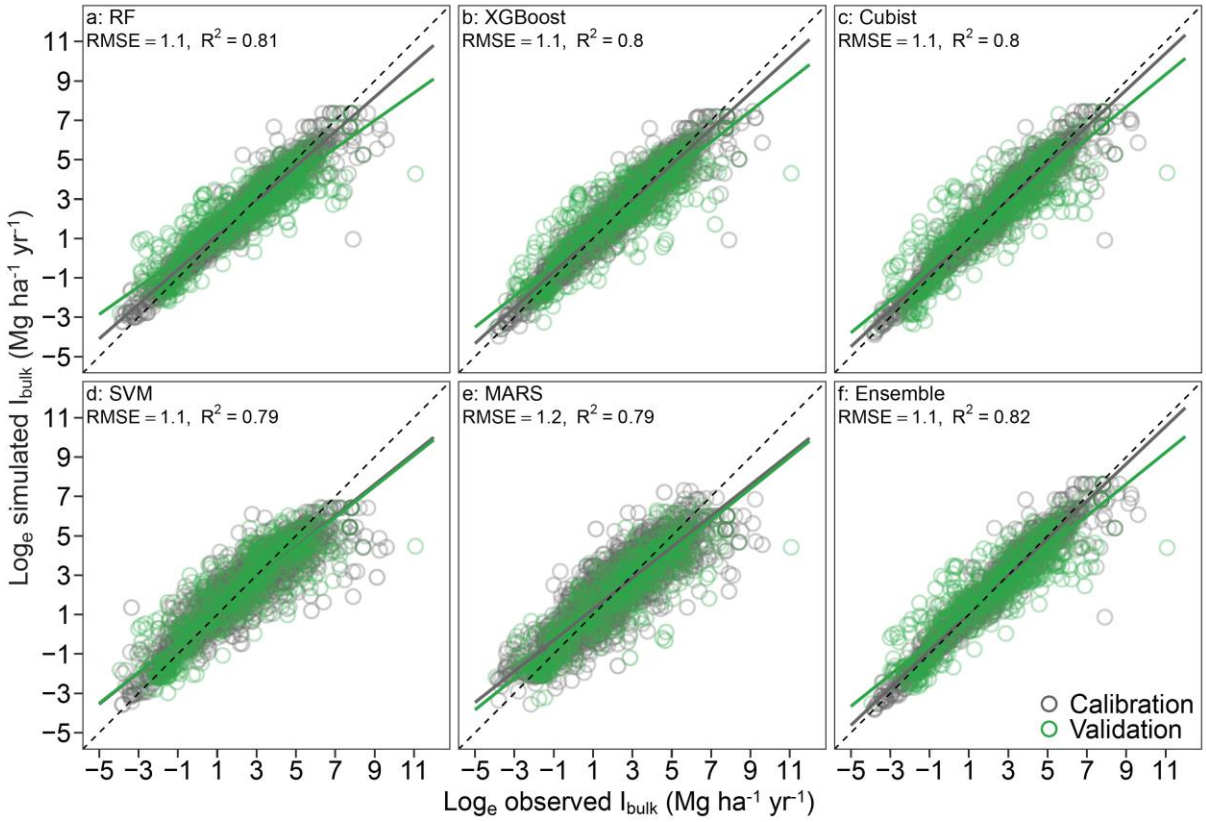

677

678 **Extended Data Fig. 3. Performance of fitted machine learning models to predict I_{bulk}.** Data
679 are log-transformed. **a**, random forest (RF); **b**, extreme gradient boosting (XGBoost); **c**, Cubist;
680 **d**, support vector machines (SVM); **e**, multivariate adaptive regression splines (MARS); **f**, the
681 ensemble model of **a**-**e**. For each individual model, 80% of the stratified samples of
682 observations were used for model calibration, with the other 20% stratified data for validation.

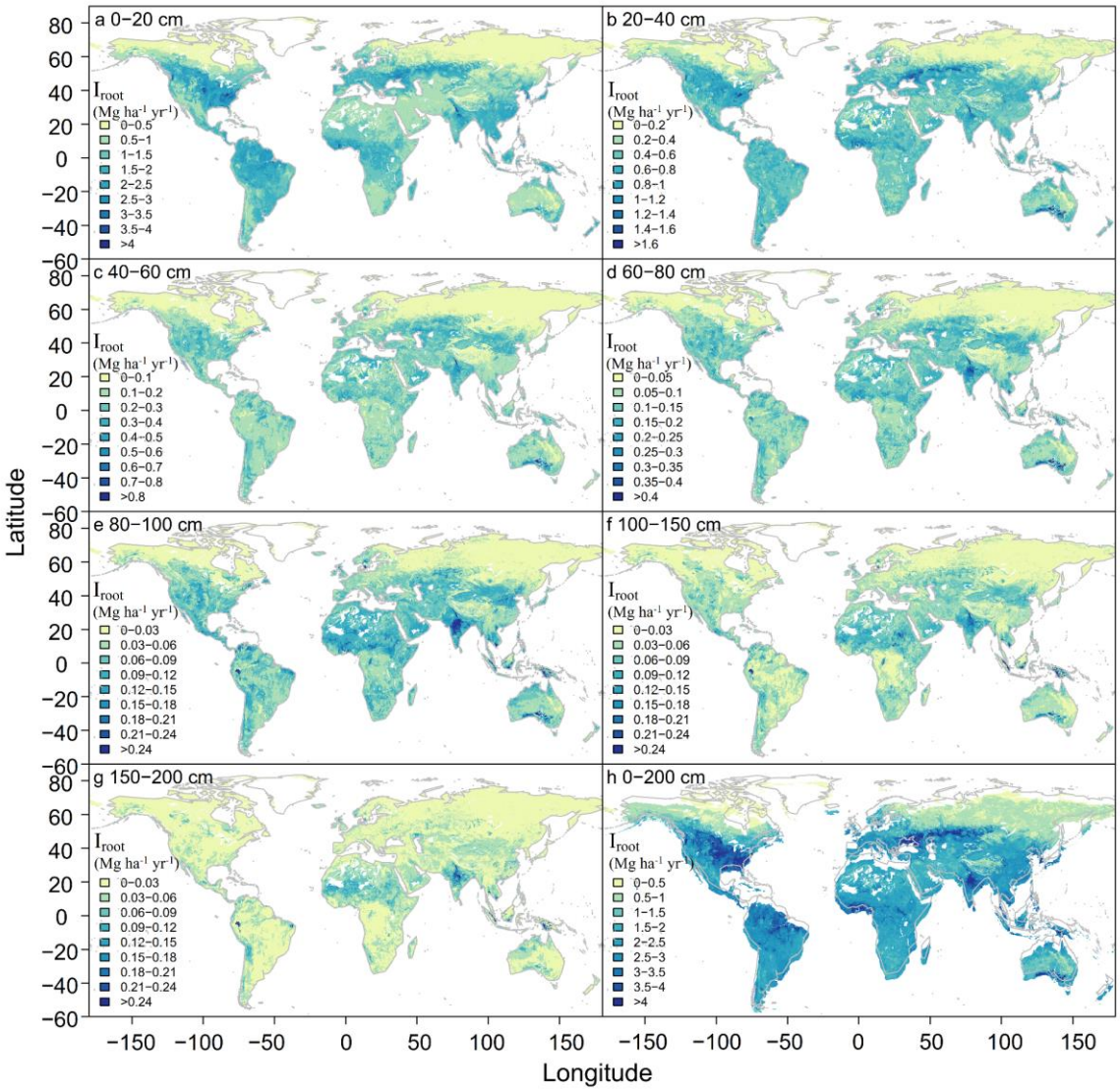

683

684 **Extended Data Fig. 4. Global pattern of root-derived C inputs (i.e., I_{root}, Mg ha^{-1} yr^{-1}) in**

685 **seven standard soil layers and in the whole soil profile (0-200 cm).**

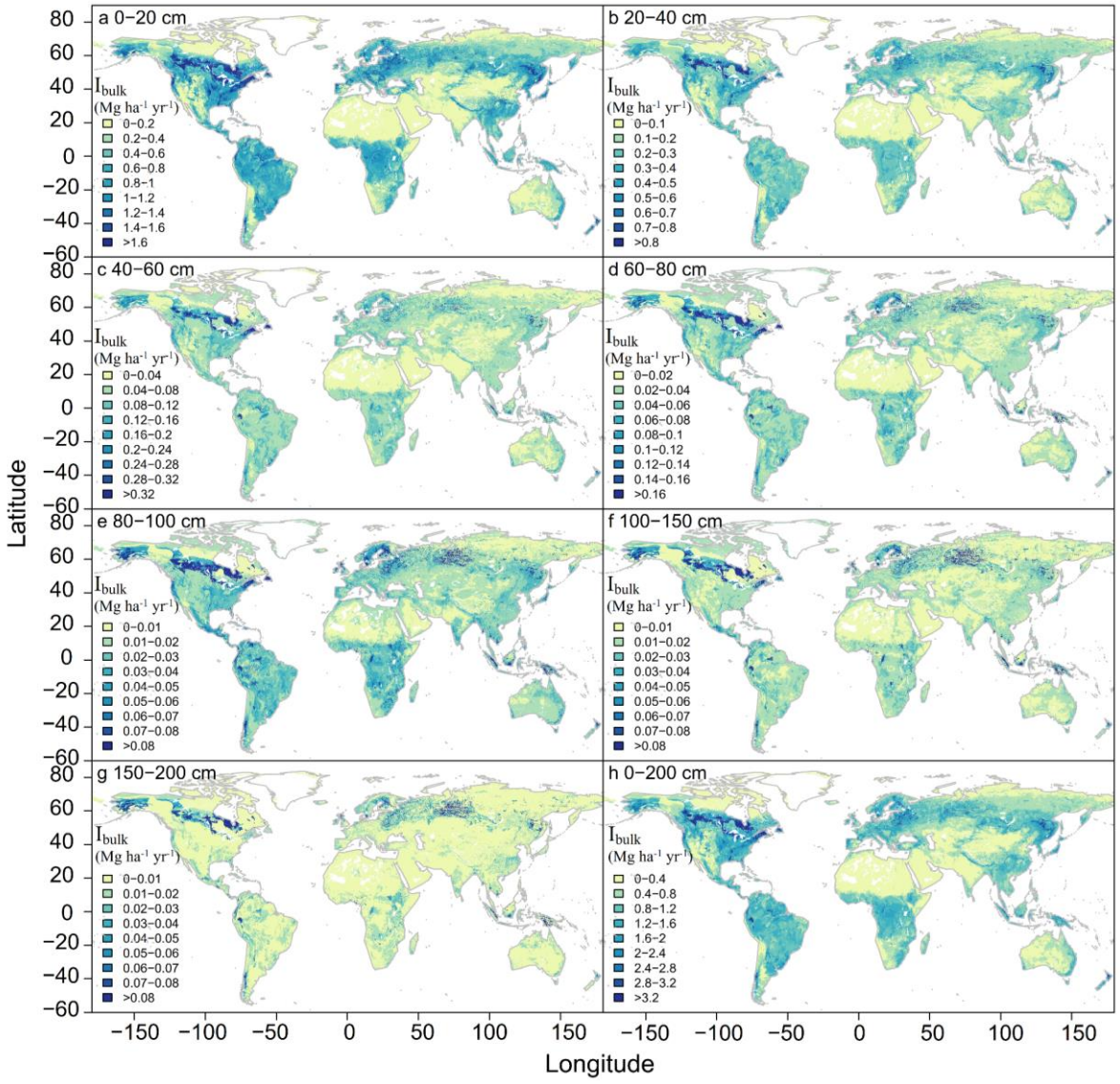

686

687 **Extended Data Fig. 5. Global pattern of actual carbon inputs to bulk soil (i.e., I_{bulk}, Mg**

688 **ha^{-1} yr^{-1}) in seven standard soil layers and in the whole soil profile (0-200 cm).**

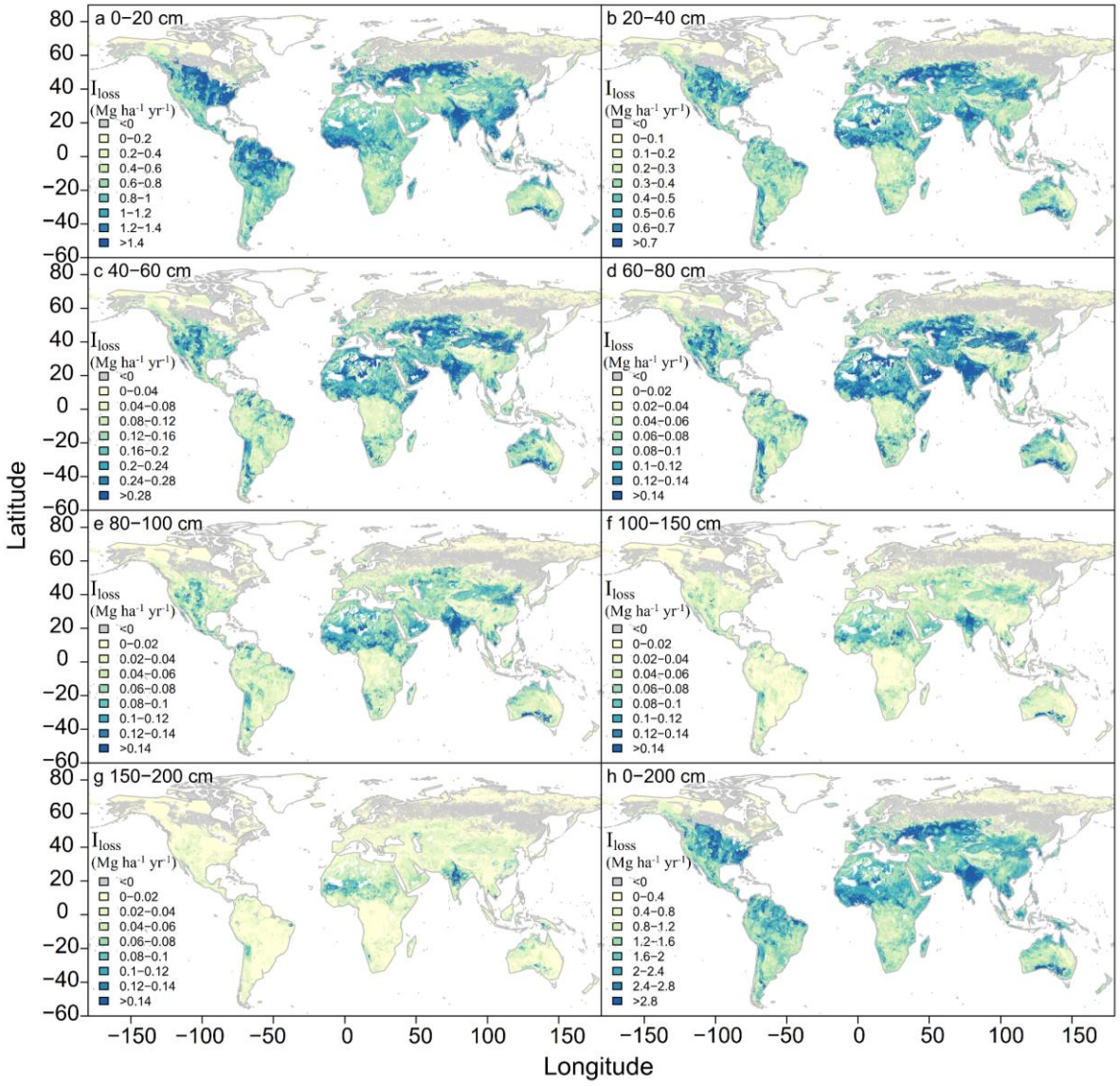

689

690 **Extended Data Fig. 6. Global pattern of direct loss of root-derived C inputs before**

691 **entering bulk soil carbon pool (i.e., $I_{loss} = I_{root} - I_{bulk}$, Mg ha^{-1} yr^{-1}).**

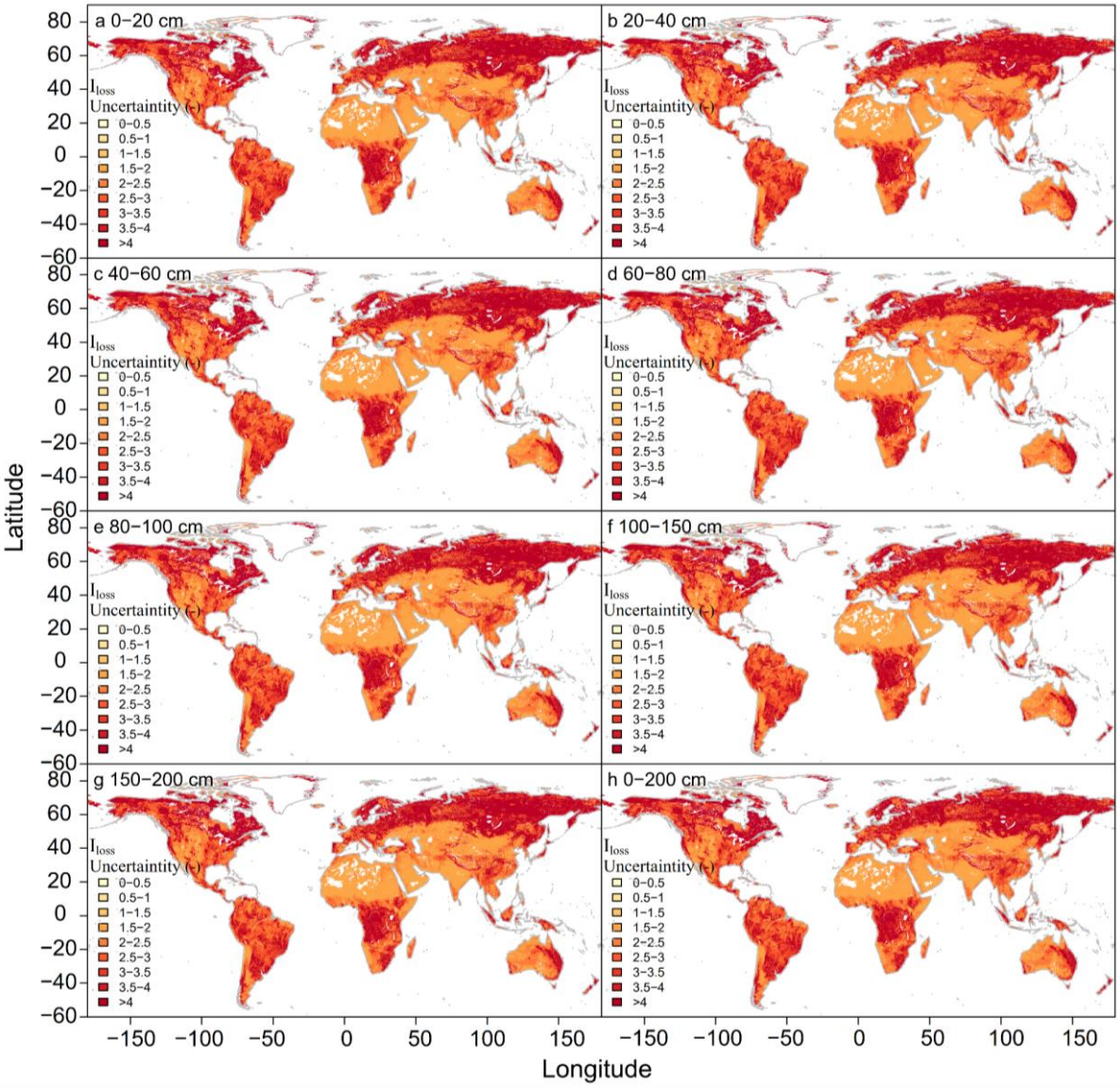

692

693 **Extended Data Fig. 7. Global pattern of the uncertainty of I_{loss} in different soil layers.**

694 Uncertainty is estimated as the margin of the deviation of 500 Monte Carlo simulations divided

695 by their mean, considering uncertainties in both observational data sets and prediction models.

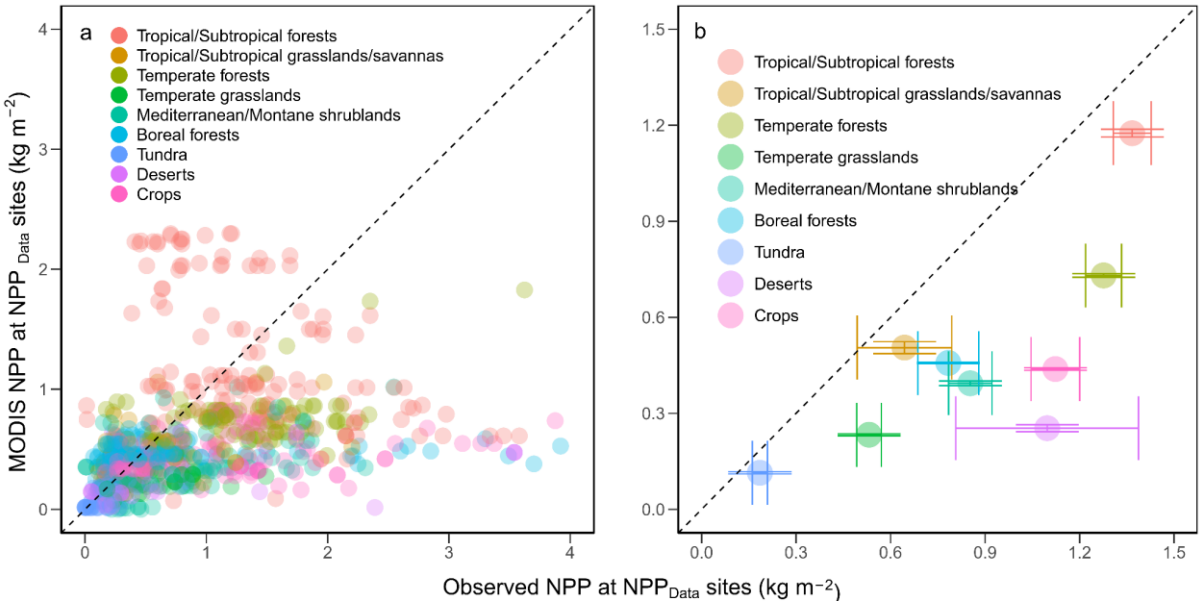

696

697 **Extended Data Fig. 8. Comparison between observed net primary production (NPP) and**

698 **MODIS-retrieved NPP at NPP_{data} sites. a**: site-by-site comparison; **b**: comparison by

699 aggregating data into nine biomes. Dashed lines show the 1:1 line.

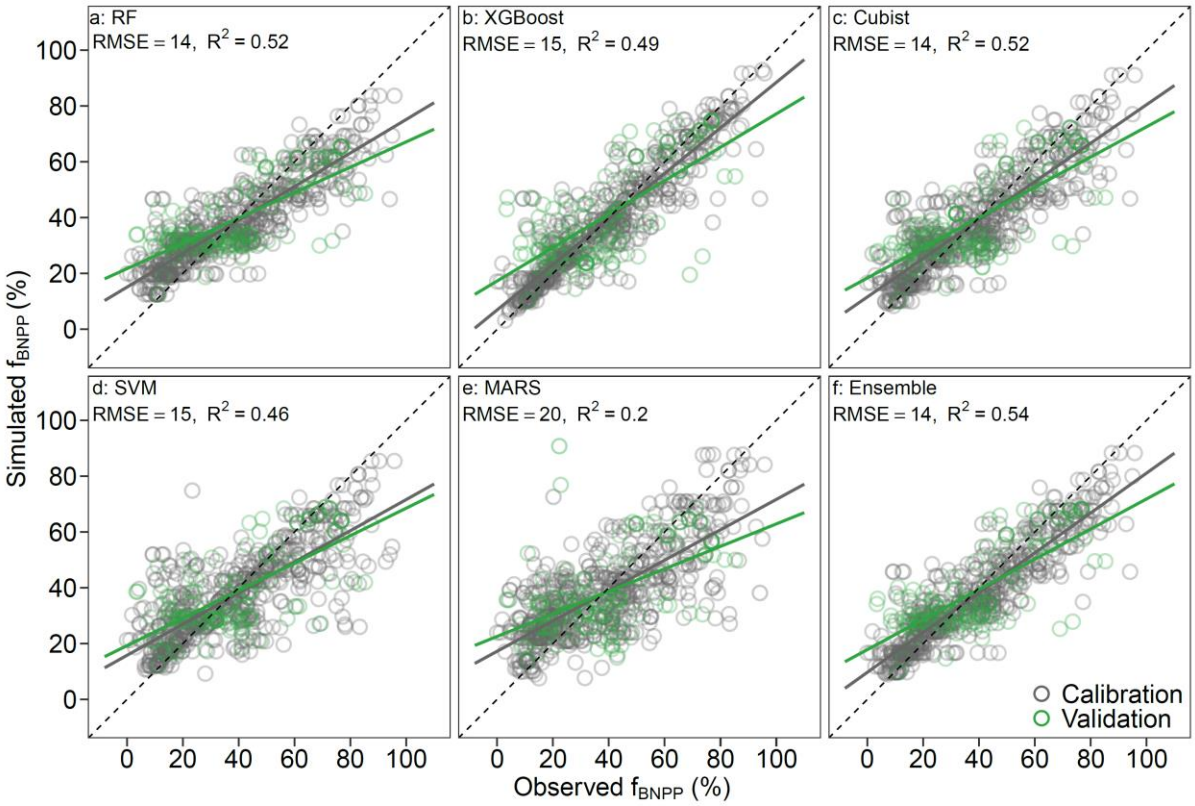

Extended Data Fig. 9. Performance of fitted machine learning models to predict the belowground fraction of NPP (i.e., f_{BNPP}). **a**, random forest (RF); **b**, extreme gradient boosting (XGBoost); **c**, Cubist; **d**, support vector machines (SVM); **e**, multivariate adaptive regression splines (MARS);**f**, the ensemble model of **a-e**. For each individual model, 80% of the stratified samples of observations were used for model calibration, with the other 20% for validation.

Supplementary information:

Supplementary Data 1: The observed above- and belowground NPP data at the 725 NPP_{data} sites (Extended Data Fig. 1).

Supplementary Data 2: The depth distribution of root biomass at the 559 $Root_{data}$ sites (Extended Data Fig. 1).

Supplementary Data 3: Estimated carbon age (C_{age}) and I_{bulk} at the 750 $\Delta^{14}C_{data}$ sites (Extended Data Fig. 1).

Supplementary Data 4: The 54 studies from which the NPP_{data} were derived.

Supplementary Tables 1-3

Supplementary Figures 1-8